Worcester Polytechnic Institute
Digital WPI

Major Qualifying Projects (All Years) | Major Qualifying Projects

April 2012

Material and Design Optimization for an Aluminum Bike Frame

Adrian Cushing Shaw
Worcester Polytechnic Institute

Forrest Potter Dwyer
Worcester Polytechnic Institute

Richard Gordon Tombarelli
Worcester Polytechnic Institute

Follow this and additional works at: https://digitalcommons.wpi.edu/mqp-all

Repository Citation
Shaw, A. C., Dwyer, F. P., & Tombarelli, R. G. (2012). *Material and Design Optimization for an Aluminum Bike Frame*. Retrieved from https://digitalcommons.wpi.edu/mqp-all/733

This Unrestricted is brought to you for free and open access by the Major Qualifying Projects at Digital WPI. It has been accepted for inclusion in Major Qualifying Projects (All Years) by an authorized administrator of Digital WPI. For more information, please contact digitalwpi@wpi.edu.

Material and Design Optimization for an Aluminum Bike Frame

A Major Qualifying Project

Submitted to the Faculty

Of the

WORCESTER POLYTECHNIC INSTITUTE

In Partial Fulfillment of the Requirements for the

Degree of Bachelor of Science

By

Forrest Dwyer

Adrian Shaw

Richard Tombarelli

April 26th, 2012

Professor Diana A. Lados

Abstract

Fatigue is a prominent failure mechanism for mountain bike frames, and can lead to serious accidents, costly recalls, and poor product image for bicycle frame manufacturers. The team collaborated with a local bike company, in the process of developing a new 6061-T6 aluminum mountain bike, to investigate the fatigue behavior of the new frame and optimize the material/heat treatment and frame design. The fatigue testing was done in-house using a test rig specifically built for this project according to the ASTM standard F2711-08 for horizontal loading. A solid model of the frame was created and a finite element analysis (FEA) was conducted using the ASTM standard as a guide, with appropriate mechanical properties for various sections of the bike and the joining welds. The FEA model enabled the team to predict fatigue failure locations and cycles to failure, and was further validated using the experimental fatigue testing results obtained from the prototype frames. On the physical frames tested, thorough fractographic examinations were conducted to identify the fatigue crack initiation locations and crack propagation mechanisms using optical and scanning electron microscopy. To complete the project, systematic studies were performed to optimize the frame's design, materials and heat treatment for improved fatigue resistance.

Table of Contents

List of Figures

List of Tables

Glossary of Acronyms

Below is a list of all the acronyms used in the report.

FEA – Finite Element Analysis

FSW – Friction Stir Welding

HAZ – Heat Affected Zone

HRE – Rockwell Hardness (E-Scale)

SEM – Scanning Electron Microscope

SSR – Solid State Relay

TIG – Tungsten Inert Gas Welding

TMAZ – Thermo-mechanically Affected Zone

UTS – Ultimate Tensile Strength

VI – Virtual Instrument

1.0 Introduction

1.1 Problem Statement

With the abusive conditions of mountain biking, bicycle riders require frames that can withstand significant forces, and have high fatigue lives. Aluminum is the material of choice for most bicycle companies when it comes to mountain bicycle frames, with other common materials being steel, titanium and carbon fiber. Aluminum has a favorable strength to weight ratio, and a lower cost compared to other materials used for bicycles. However, when compared to these other materials, aluminum is more susceptible to fatigue failure at lower cycle counts and has a finite fatigue life. Fatigue failures that occur during typical usage of mountain bikes can have devastating effects for bicycle manufacturers, resulting in expensive recalls, legal liabilities, and loss in product image [30]. Table 1 outlines the major recalls in aluminum bicycle frames from 1995-2010 due to fatigue failure.

Table 1: Bicycle frame recalls between 1995 and 2010

Year	Company	Failure	Result	Ref.
2010	Niner Bikes	Cracks in welds in front triangle of frame	Recall of 750 frames	[31]
2010	Redline Bikes	Cracking in head tube weld joints of aluminum frame, separation of head tube	Recalls	[36]
2009	Norco Bicycles	Cracking in head tube area of aluminum frame, head tube separation	Recall of 3600 frames	[32]
2005	Novara	Fatigue failure in head tube region	Recall of 2800 frames	[13]
1995	Cannondale	Cracks in head tube region	Safety inspections	[12]

Based on the many recalls summarized in Table 1, the group decided to investigate fatigue failures occurring in the front triangle of aluminum mountain bike frames.

1.2 Project Objectives

Three main objectives were followed to investigate fatigue failures in the front triangle of bicycle frames. These objectives work towards investigating the fatigue life and failures of aluminum bicycle frames. The first main objective involved using finite element analysis (FEA) to develop an integrated methodology to predict fatigue failure locations and fatigue lives at those locations. Fatigue failure locations and fatigue lives are critical considerations for bicycle frame design.

The second objective of the project was to validate the FEA methodology using physical frame testing. Validating the FEA methodology with physical testing allows for determining whether the predicted fatigue failure locations and cycles to failure are accurate. The last main objective involved optimizing material, heat treatment and geometry to improve fatigue life. The material selection, heat treatment and geometry of a bicycle frame all have a significant impact on the fatigue failure locations, and cycles to failure.

1.3 Methodology Overview

After defining the main objectives to investigate fatigue failures, the group determined it was necessary to obtain a physical bicycle frame to analyze and optimize.

The group found a local bicycle company willing to donate two identical 6061-T6 aluminum prototype mountain bike frames for a fatigue investigation. The investigation not only met the objectives of the group, but also provided value for the local bicycle company by testing and validating the fatigue life of the prototype.

The group devised an integrated FEA methodology to understand the fatigue behavior of the bicycle frame. The FEA methodology was based on the bicycle specific ASTM F2711-08 test standard. The methodology allowed the group to use computer simulation to predict the fatigue failure locations of the donated frames, and the cycles to failure in those locations. The FEA methodology was then validated using physical frame testing. A fatigue testing rig was built in-house to test one of the donated frames until failure. The second frame was sent out to an external testing facility to ensure the group obtained accurate fatigue testing data. The results between the physical frame testing were compared to the FEA methodology results to determine how well the FEA methodology agreed with actual testing.

The fatigue crack on the tested frame at WPI was then fractographically analyzed to obtain an understanding of the crack propagation. An optical microscope and a scanning electron microscope (SEM) were used to analyze the fracture. The analysis was compared and correlated to the observed crack growth rate. A point of origin was found using the SEM to determine exactly where and why the crack originated.

After developing the FEA methodology, validating the methodology, and conducting the fractographic analysis, the group worked to optimize the material, heat treatment and geometry design of the frame. Changes were made to each of these characteristics of the frame to work to optimize the fatigue life. Alternative aluminum

alloys were investigated as well as alternative heat treatments of 6061 aluminum for the bicycle frame. Finally, modifications to the frame geometry were made to work to improve the fatigue life of the frame. The material, heat treatment and geometry modifications were then combined to result in a bike frame optimized for fatigue resistance.

2.0 Characterization of Donated Frames

This project involved an investigation into fatigue failures of aluminum mountain bike frames. As discussed in Chapter 1, two 6061-T6 aluminum mountain bike frames were donated from a local bicycle manufacturer for an investigation into fatigue failure locations and fatigue life. The donated frames can be seen in Figure 1. This chapter provides a characterization of the frame tubes of the donated frames, an overview of the material properties of the frames and a characterization of the process for manufacturing the donated frames.

Figure 1: Donated mountain bike frame.

2.1 Frame Tubing Characterization

The bicycle frames donated for fatigue investigation feature a traditional diamond frame design, consisting of a front and rear triangle. This design has been the industry standard for bicycle frame design for over one hundred years [10]. The frame consists of a top tube, down tube, head tube, seat tube, seat stays, and chain stays as seen in Figure 2. The head tube of the frame holds the steerer tube of the fork, which in turn holds the front wheel. The top tube and down tube connect the head tube to the seat tube and bottom

bracket. The seat tube holds the seat post, which holds the saddle. The bottom bracket holds the cranks, which hold the pedals. The seat stays and chain stays hold the rear dropouts, which connect the rear wheel to the frame [40].

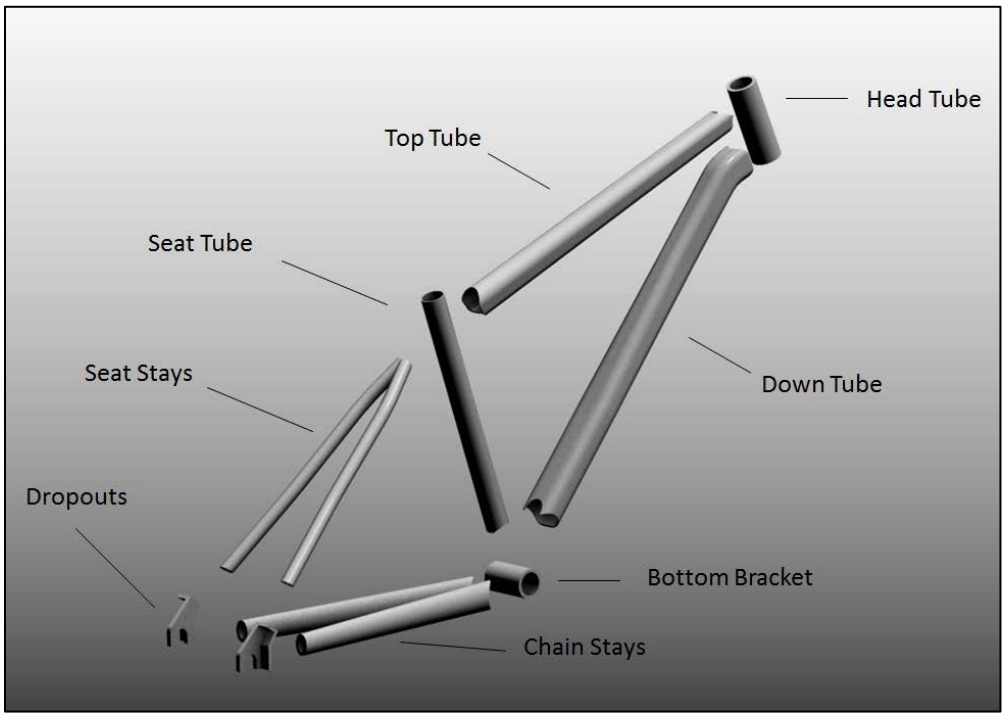

Figure 2: Tubing diagram of the donated bicycle frames.

2.2 Material Properties Characterization

The bicycle frames donated for investigation are made from 6061 aluminum with a T6 heat treatment. This section covers the material properties of 6061-T6 aluminum in comparison to other common bicycle frame materials.

There are a wide variety of materials used in bicycle frames. Bike frames were originally made from wood, but modern frames are made primarily from aluminum, steel, titanium and carbon fiber. Some of the less common materials used in creating frames

include bamboo, thermoplastics and magnesium. Bicycle frames constructed from the more common frame materials can be seen in Figure 3.

Figure 3: Common bicycle frame materials [20],[37],[21],[43].

The materials used for mountain bicycle frames have a wide range of mechanical properties. These properties can be seen in Table 2. There is not one material in the table that has advantageous properties in each category, which explains why manufacturers continue to fabricate frames from several different materials.

Table 2: Mechanical properties of common bicycle frame materials [16], [26]

	Modulus of Elasticity (GPa)	Yield Strength (MPa)	Tensile Strength (MPa)	Fatigue Strength at 50,000 Cycles (MPa)	Density (kg/m^3)	Weldability and Machinability	Cost (USD per kg)
Aluminum – 6061-T6	72	193-290	241-320	75	2,700	Excellent	$2.42
Aluminum – 7005-T6	72	290	350	~75	2,780	Excellent	$2.87
Steel - 4130	205	800-1,000	650	250	7,800	Excellent	$0.95
Titanium – Grade 9	91-95	483-620	621-750	250	4,480	Fair	$57.40
Carbon Fiber	275-415	Varies	Varies	Varies	1,800	Fair	Varies

2.2.1 6061-T6 Aluminum

The 6061 aluminum alloy is an alloy commonly used for a wide variety of applications. This material is used for bicycle frames, aircraft structures, automotive parts, and much more [18]. The two main alloying elements in 6061 are silicon and magnesium. The complete composition of 6061 can be seen below in Table 3.

Table 3: Approximate chemical composition of 6061 by wt% [16]

Al	Mg	Cr	Cu	Si	Fe	Mn	Zi	Ti
~96.5	1.0	0.2	0.4	0.6	0.7	0.15	0.25	0.15

The 3D models of the grain structure of 6061-T6 aluminum can be seen in Figure 4. The models show the grain structure of the top and down tubes respectively. The two models allow for an understanding of the orientation of the grains with respect to the crack propagation. The T, L, and S directions refer to the transverse, longitudinal and short-transverse directions of the tube respectively. As can be seen in the figure, the down tube features smaller grains, which contributes to higher material yield strength in the down tube [27].

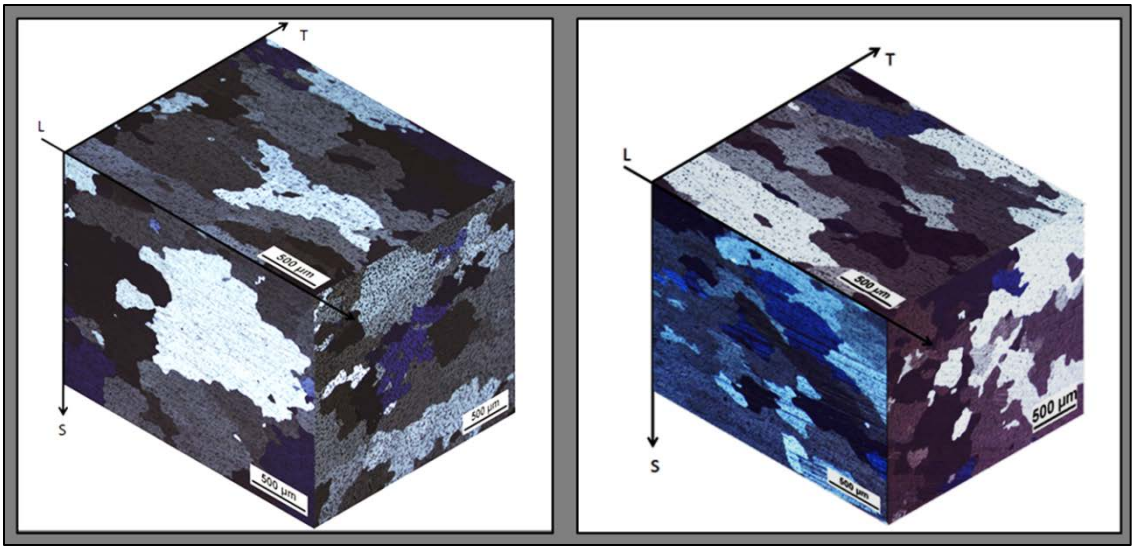

Figure 4: 3D grain models showing top tube (left) and down tube (right).

From the previous figure, the most apparent difference between the top tube and down tube is that the grains on the down tube are smaller. This affected the fatigue behavior of the bicycle frame, and is further explained in Chapter 4. Another aspect that affected fatigue behavior is that the grains in the LS and TS plains are longitudinally elongated. These grains are considered aqueous due to their aspect ratio of roughly 2:1. Also, on the TS planes of both tubes, the grains appear smaller. Both of these occurrences can be attributed to the manufacturing process of the material. As further explained in Section 2.3, the frame tubes were extruded then hydroformed which gives them this distinct grain orientation.

2.2.2 Aluminum 6061 Compared to Other Frame Materials

As seen in Table 2, each frame material, including 6061, has advantages and disadvantages when compared to the other materials. The important mechanical

properties for comparing bike frame materials include the material's density, tensile strength, fatigue strength, weldability and cost. Aluminum 6061 has the second lowest density compared to the other materials, with a density that is 60% that of titanium, and 35% of 4130 steel. The tensile strength of 6061 is less than 7005, and around 43% of 4130 steel and titanium. The low density of aluminum allows larger tube diameters to be used to increase frame strength making it to be competitive and even advantageous when compared to steel. The main drawback to titanium, as shown by Table 2, is the tremendously high cost, making the material less common for bicycle frames. Aluminum 6061 is more expensive than steel, but is relatively inexpensive at around $2.43 a kilogram, making it affordable for manufacturing a frame. The main drawback to aluminum is the low fatigue strength compared to the other frame materials.

Fatigue Comparison

Fatigue strength and resistance to fatigue failure is a highly important property when comparing common bicycle frame materials. Fatigue failure is defined as the progressive, localized, and permanent structural change that occurs in a material subjected to fluctuating stresses below the yield strength. Riding a bicycle produces fluctuating stresses on the frame that in some cases, cause fatigue failures to occur. As seen in Table 2, the aluminum alloys have much lower fatigue strengths when compared to 4130-steel and titanium, and are thus much more susceptible to fatigue failure. This means that 6061 requires much lower stresses and cycles to induce a fatigue failure. Both steel and titanium have fatigue strengths of 250 MPa at 50,000 cycles while the aluminum alloys have fatigue strengths of only about 75 MPa at 50,000 cycles.

The 4130 steel alloy and titanium also have a fatigue limit which aluminum does not. Fatigue limit is defined as the range of cyclic stresses that a material can undergo without the material experiencing fatigue failure. From the data in Figure 5, it is clear that after 10^5 cycles, the theoretical endurance limit of steel is 300 MPa. This means that, as long as the steel is not stressed past 300 MPa, it will never suffer fatigue failure. From this graph it can also be seen that the strength of aluminum falls continuously and has no fatigue limit. Ideally bicycle frames would be designed to operate with stress levels below the endurance limit; since aluminum does not have an endurance limit, fatigue failure is prevalent issue as failure is guaranteed to happen after a finite number of cycles [16].

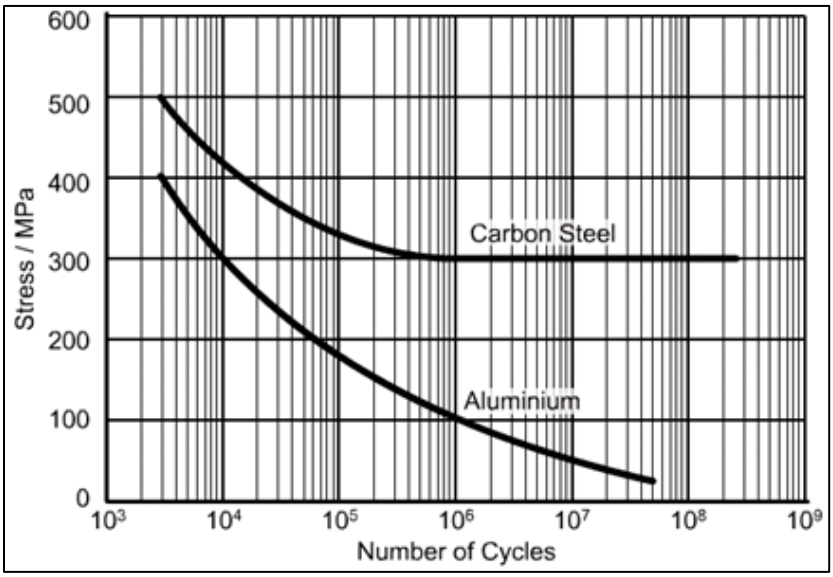

Figure 5: Fatigue limit of aluminum vs. steel [19].

Aluminum has a number of properties that make it more desirable when compared to other materials such as low density, ease of welding, good strength when heat-treated

and high corrosion properties as described above. As shown above, the main drawback to 6061 frames is the susceptibility to fatigue failures.

2.2.3 Aluminum 4043 – Filler Rod

The 4043 aluminum alloy was used as the filler rod for welding the donated frames. The ASM recommends 4043 filler material when welding 6061, and it accounts for a large portion of the weld material [45]. The higher silicon content in 4043 weld wire (5% vs. 0.6% in 6061) makes welds less sensitive to weld cracking which is why 4043 is so widely used. The high silicon content also leads to excellent wetting during welding. Wetting is the process in welding where the liquefied filler material flows over the base metal. The complete chemical composition of 4043 can be seen in Table 4. Important mechanical properties of 4043 include a tensile strength of 140 MPa and yield strength of 55.2 MPa. Furthermore, 4043's relatively low solidification temperature of 575°C is ideal for welding 6061 as it reduces the occurrence of liquidation cracking during welding [16].

Table 4: Approximate chemical composition of 4043 filler rod by wt% [16]

Al	Si	Fe	Cu	Ti	Zn	Mn	Mg	Others
~93	5	0.80	0.30	0.20	0.10	0.05	0.05	0.15

2.3 Manufacturing 6061 Aluminum Bicycle Frames

There are four main steps in manufacturing the aluminum bicycle frames donated for the project which are shown in Figure 6. As seen in the figure, extruded aluminum tubes are hydroformed, miter cut, tungsten inert gas (TIG) welded then T6 heat treated.

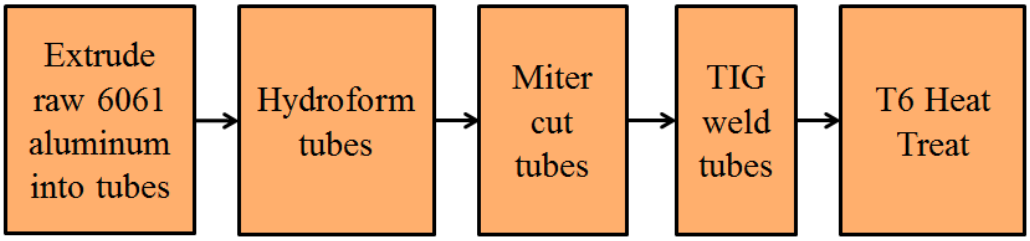

Figure 6: Manufacturing process for an aluminum bicycle frame.

2.3.1 Creation of Blank Tubes

The first step in creating a bicycle frame out of 6061 aluminum is to create the individual tubes that make up the frame. Aluminum tubes are created through a process known as extrusion. The first step in extrusion is to obtain an aluminum slug. An aluminum slug is a small, circular piece of aluminum that looks similar to a coin. This slug is pushed into a die which forces the slug to take the shape and diameters of the desired tube. After a sufficient amount of material is through the die, the end that is through is threaded so that it can be further pulled through. Once a sufficient enough amount of tube is created it is cut both at the die as well as at the cap where the threading is to create a tube of desired dimensions. After the tubes are cut to the correct length, they must then be further altered before assembly to ensure proper fit and proper strength properties [3].

2.3.2 Altering the Tubes

The most common methods for altering blank bicycle tubes are hydroforming and mitering the tubes. For hydroforming, the blank tubes with circular cross sections are altered to yield a more complex and stronger geometry. The concept of the hydroforming process is simple, and requires only a steel die and a fluid. The blank tube is placed in the die and the ends of the tube are sealed off. Fluid, usually water, with an anti-corrosive additive is then pumped into the tube at high pressure. This forces the tube to expand and thereby conform to the shape of the die. With hydroforming, fluid pressures can often exceed 135 MPa [25]. A diagram of the tube hydroforming process is shown in Figure 7.

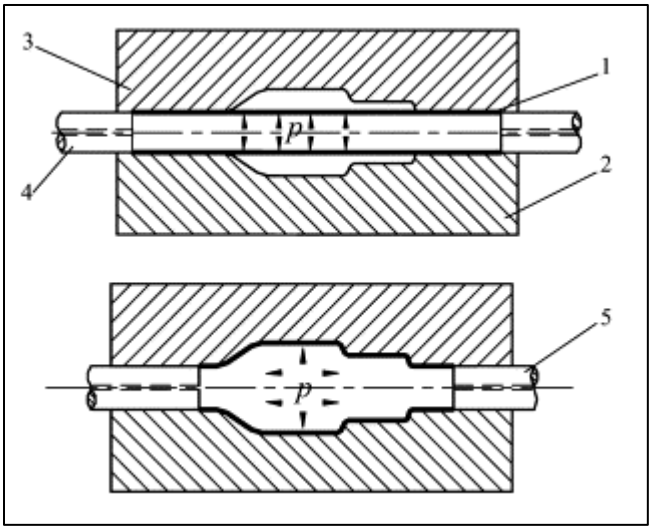

Figure 7: Hydroforming a blank tube using a die and high pressure fluid [25].

In order for tubes to easily and securely connect to one another in the shape of a frame, they must be miter cut. By mitering the end of a tube, two tubes can be joined together in a seamless fashion, making the joint stronger. A machine specifically

designed for tube mitering is used most often which produces a clean and accurate cut. Mitering also allows the ends of tubes to sit flush with the sides of the tubes that it will eventually be joined to [22]. An example of a miter cut tube is shown in Figure 8.

Figure 8: A bicycle tube which has been miter cut [22].

After mitering, the tubes must be joined together. When fabricating an aluminum bicycle frame, there are a number of different options for joining tubes. The three most common joining processes are welding, adhesive bonding, and mechanical fastening. The frames that were tested by the group utilized TIG welding for construction.

2.3.3 Joining the Tubes: TIG Welding

Welding is the method of choice for most manufacturers to join frame tubes, as it provides high joint strength and is also affordable. TIG welding is the most common type of welding for 6061 bicycle frames, and was the joining method used for the donated frames. A photo of this process can be seen in Figure 9. TIG Welding is an arc welding process in which heat is produced between a non-consumable tungsten electrode and the

work metal. TIG welding utilizes the inert gas, argon, to keep the weld area clean which prevents the metal from oxidizing during the welding process. TIG welding is commonly chosen as the welding method for thin tubes and is desirable for the bicycle industry since it provides a high quality finish on the weld surface [2]. Aluminum 4043 filler rod was used during TIG welding of the donated frames.

Figure 9: TIG welding the head tube of an aluminum bicycle frame [38].

Consequences of TIG Welding

The major consequence of TIG welding is the change in the physical properties of the base material and weld due to the heat applied to the fusion zone. A small area around the fusion zone known as the heat-affected zone (HAZ) exhibits the worst change in properties and as a result, fatigue failures will often propagate from the HAZ. A diagram showing the location of the HAZ can be seen in Figure 10 with the filler material in red and the HAZ in grey. The HAZ is subjected to extreme temperature change during the welding process which causes the growth of precipitates. The precipitates decrease the hardness and therefore degrade the mechanical properties such as ultimate tensile strength by as much as 34%. For example, with 6061 the tensile strength before welding

is 310.3 MPa. After welding, the HAZ has a tensile strength of 186.2 MPa. This drastic loss in strength due to the welding process can seriously affect the life of an aluminum bike frame [23].

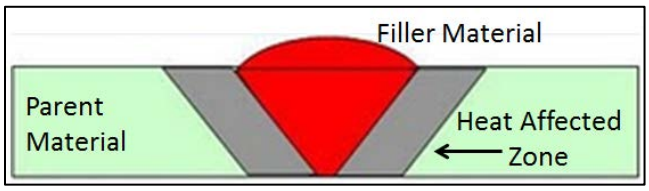

Figure 10: Zones of a TIG weld showing parent material, HAZ, and filler material.

However, there are alternative welding techniques to TIG welding that produce welds with less substantial heat affected zones. One of these welding methods is Friction Stir Welding (FSW). FSW involves using a non-consumable tool with downward pressure to produce the weld, avoiding melting the base material and using lower heat compared to TIG welding. This process creates a number of zones including the weld zone, thermo-mechanically affected zone (TMAZ) and a HAZ as seen in Figure 11. These zones exhibit mechanical properties that are generally poorer than the parent material, but are better than the properties produced using conventional TIG welding. Although FSW welding may be practical for use on 6061 bicycle frames, the technology has not been explored for this application yet, and thus the HAZ created by TIG welding is still an issue for aluminum bicycle frames [42].

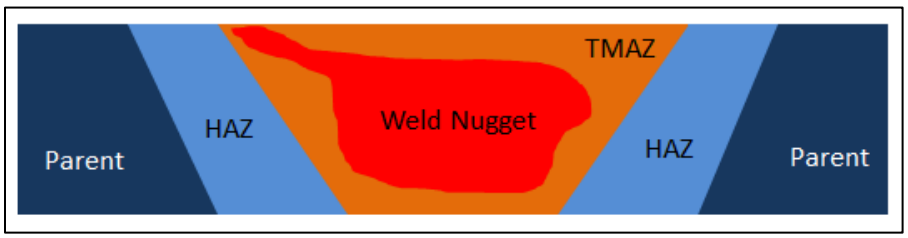

Figure 11: FSW diagram showing parent material, HAZ, TMAZ and weld nugget.

2.3.4 T6 Heat Treatment of 6061 Aluminum

After aluminum frames are TIG welded, the frames are heat treated in an effort to recover the mechanical properties that are lost during TIG welding. Heat-treating is a term used in manufacturing to describe the changing of the metallurgical structure, residual stress state, and mechanical properties of a metal by heating and cooling. With aluminum alloys specifically, the term heat-treating describes increasing the strength and hardness of precipitation-hardenable wrought alloys. The bicycle frames donated for investigation in this project were T6 heat-treated. T6 heat-treating is considered an optimal operation for recovering the mechanical properties of 6061 after TIG welding [17]. The steps for the T6 heat-treatment of the donated frames can be seen in Figure 12.

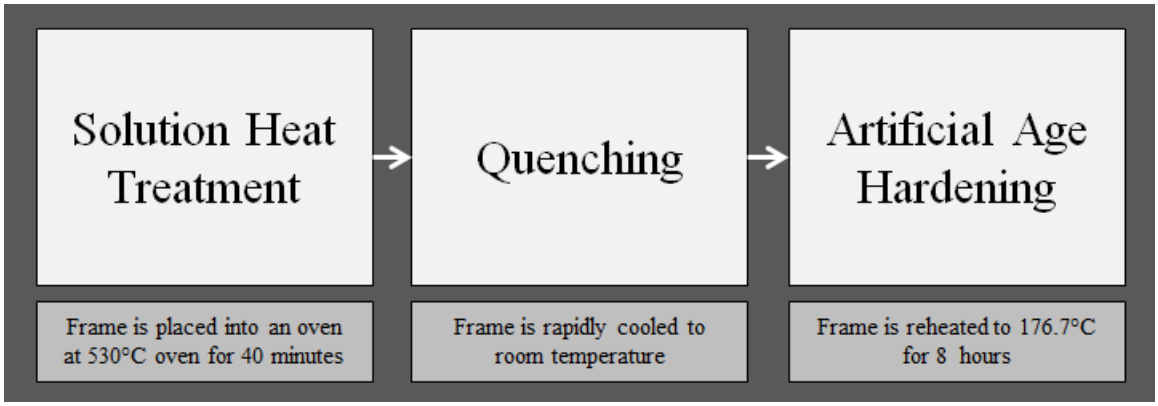

Figure 12: T6 heat treatment process steps [17].

Solution heat treatment causes the dissolution of soluble phases to get a virtually homogenous solid solution to form. The soak time for solution differs depending on the thickness of the piece of aluminum undergoing the solution heat treatment and can be seen in Appendix A [17]. At the completion of the solution heat treatment phase, 6061 is designated to be T4 heat treated.

In order to raise the temper designation from T4, quenching, which is considered to be the most important step in the entire process, is utilized. The purpose of quenching is to ensure the preservation of the solid solution formed at the high temperatures of the solution heat treating process. In general, the higher the quenching rate, the higher the material strength will be. This process must be started with a delay of only a few seconds, since as the alloy leaves the furnace it begins to lose the strengthening properties gained in the solution heat treating phase [17].

The last step in completing the T6 heat treat process is known as artificial aging. This process achieves the precipitation of solute atoms and serves to relieve residual stresses in the material up to 35%. Without both solution heat treating, and quenching, this process would not be possible. The two prior processes allow for the precipitates to form during the artificial aging phase. These precipitates are what add to the final strength of the alloy and are the key to the T6 heat treat process. The size of these precipitates can be adjusted by changing both the temperature and time of the aging. For 6061-T6 the optimum precipitate size and thus optimum final strength is achieved by placing the alloy into a furnace for 8 hours at 176.7°C. The entire heat treating process allows 6061 to recover 30% of the pre-weld tensile strength [17].

A thorough understanding of the frame design, materials, and manufacturing processes provided the group with the necessary background to conduct an analysis on the bike frames, with a specific focus on fatigue behavior.

3.0 Frame Analysis and Testing

The group developed an integrated FEA methodology to predict the fatigue failure locations and cycles to failure for those locations. The FEA outputs were then validated using physical frame testing. This ensured that accurate results could be predicted with the FEA model. The ASTM F2711-08 test standard was chosen as the basis for both the FEA model and physical frame testing due to the likelihood of fatigue failures in the upper front triangle region. This test standard, followed by the FEA methodology and the physical testing, is described below.

3.1 ASTM Frame Testing Standards

The ASTM F2711-08 test standard was chosen as the standard to follow for the FEA and physical frame testing. This test standard allows for accurate simulation of real world frame use to investigate failures. The test standard is comprised of the following tests.

Horizontal Loading Durability Fatigue Test: This test involves loading the bike frame at the bottom of the front fork along the x-axis in a cyclic manner with a pre-determined load. The rear dropouts of the frame are restrained, and the front is mounted to a test fork in place of an actual fork. The test standard stipulates that the test fork must not exhibit failure before the tested frame. This test simulates fatigue loading of the frame to produce fatigue failures. This test is further discussed in Section 3.1.1.

Vertical Loading Durability Fatigue Test: This test involves loading a bicycle frame vertically just behind the seat post in a cyclic manner with a pre-determined load.

In this test the rear dropouts are restrained, and the front fork is allowed to roll. This test simulates fatigue loading of the frame to produce fatigue failures [6].

Impact Strength Test: This test involves mounting the bicycle frame vertically with a 22.5 kg striker on a test fork attached to the bicycle frame. The frame is rigidly mounted at the rear axle, and the front axle is allowed to roll. This test simulates an impact occurring on the front fork of the bicycle [6].

3.1.1 Horizontal Loading Durability Fatigue Test

The horizontal loading durability fatigue test was chosen as the test standard to follow for frame analysis. This test standard was chosen as it allows for investigation of fatigue failures in the front triangle of bicycle frames which as described in the problem statement was the area of focus for this project. The setup and positioning of the frame for this test are shown in Figure 13 [6].

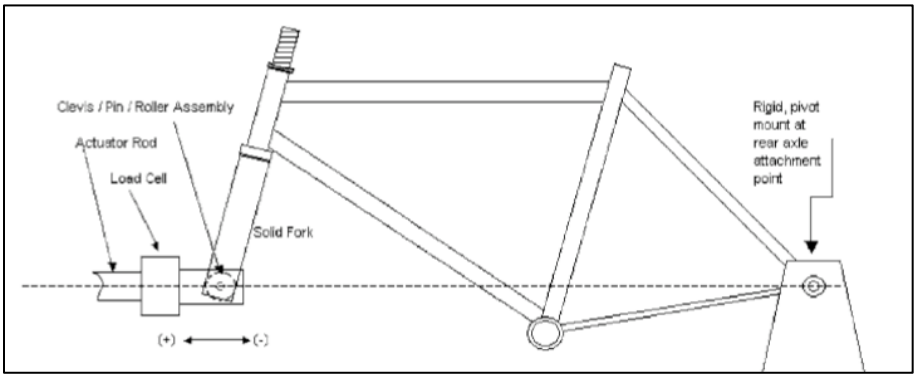

Figure 13: Test setup for the Horizontal Loading Durability Fatigue Test [6].

F2614-09 Fatigue Test Requirements

Although the ASTM F2711-08 test standard discusses how to conduct the Horizontal Loading Durability Test, it does not specify any of the testing parameters such as the loading and the number of cycles required for a frame to pass. This is because ASTM testing parameters are based on the classification of use that the bicycle frame falls under. The F2043-09 ASTM standard classifies bicycle usage into five classes of use. These classes of use can be seen in Table 5. The F2843-10a, F2802-09, F2868-10, and F2614-09 ASTM standards define the required cyclic loading for the Horizontal Loading Durability Test for classes 0-3 respectively. The standards also discuss the number of cycles that a frame must withstand in order to pass the test. Of note, condition 4 frames do not have their own standard as they are considered extreme off road bicycles, and as such there is no expectation of the forces that they will be able to withstand. A complete list of the loading for all of the conditions can be seen in Table 5.

The bicycle frame being investigated by the group falls under the Condition 3 category. As a Condition 3 bicycle, the frame is required to withstand 1,200 N of tensile force and 600 N of compressive force for at least 50,000 cycles.

Table 5: ASTM bicycle conditions and F2711-08 test parameters [4],[8],[7],[9],[5]

Condition	Intended Use	Cyclic Tensile Load (N)	Cyclic Compressive Load (N)	Cycles
Condition 0	Children's bikes	600	300	50,000
Condition 1	Paved roads and smooth surfaces	600	600	100,000
Condition 2	Unpaved and gravel roads	800	600	50,000
Condition 3	Rough technical areas, unimproved trails, small jumps	1,200	600	50,000
Condition 4	Extreme off road riding	Undefined		

The F2843-10a, F2802-09, F2868-10, and F2614-09 ASTM standards also define the rate at which the loads are cycled during testing. Fatigue failures can be broken down into two categories: high cycle fatigue and low cycle fatigue. High cycle fatigue is defined as a failure that occurs from 10^5 to 10^8 cycles. High cycle fatigue tests are generally conducted at frequencies greater than 1,000 Hz, making them unsuitable for bicycle testing. Low cycle fatigue failures on the other hand are failures that occur from 10 to 10^5 cycles. These cycles generally occur at a rate of 1 Hz or lower [24]. By the previous definition, the Horizontal Loading Durability Test is a low cycle fatigue test with a specified rate of 1 Hz. This test frequency is an accurate representation of the fatigue loading that a bicycle sees in real world conditions.

3.2 FEA Methodology

In order to determine fatigue behavior, an FEA methodology was developed to predict fatigue failure locations and cycles to failure. The methodology is comprised of taking accurate dimensions from the donated frames, using the dimensions to build a solid model, gathering accurate material properties off of the donated frames, and then building a FEA model, with localized meshing control. The methodology for building the FEA model is overviewed in Figure 14.

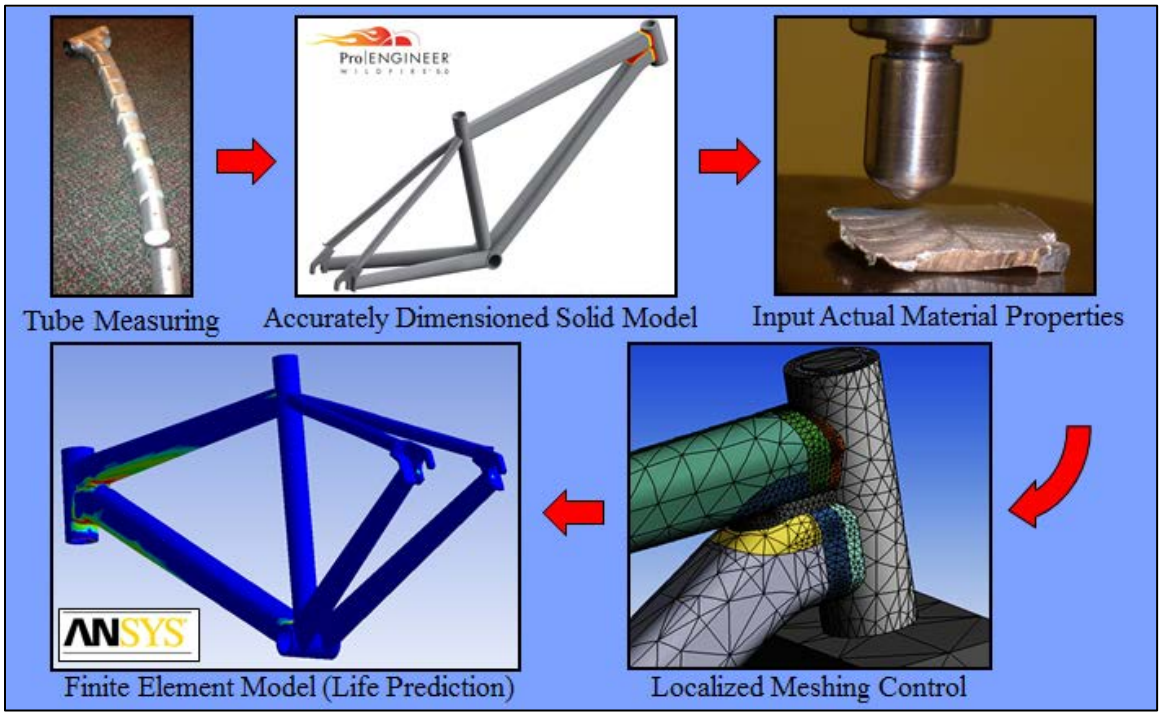

Figure 14: Integrated FEA methodology overview.

3.2.1 Tube Measurements and Solid Model Creation

Dimensions were taken to build an accurate solid model of the donated bicycle frame. The solid model was built using PTC ProEngineer. As seen in Figure 15, the creation of the solid model mimicked the actual manufacturing process for building the bicycle frame, to allow for simple and accurate creation of the solid model. The actual manufacturing process of the frames is described in Section 2.3. The solid model of the frame was developed to be an accurate representation of the donated frame, and to allow for modifications to be made to optimize the frame.

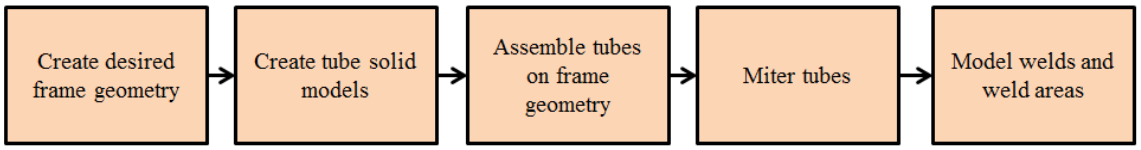

Figure 15: Bicycle frame solid modeling strategy.

Tube Geometry

Frame geometry dimensions were taken from the donated frames to characterize the overall tube layout geometry. The dimensions taken are standard dimensions used to characterize the geometry of the frame. These dimensions can be seen in Table 6. The frame geometry parameters characterize the placement and length of each of the bicycle frame tubes discussed in Chapter 2. These parameters are used by virtually every bicycle manufacturing company to characterize a frame's geometry.

Table 6: Geometry values for the solid model of the bicycle frame [37]

Parameter	Value
Head tube angle	68.5 degrees
Seat tube angle	72 degrees
Seat tube length	44.5 cm
Top tube length	59.7 cm
Chain stay length	42.4 cm
Head tube length	12.7 cm

Using these parameters, the geometry base sketch was made in ProEngineer. This sketch, shown in Figure 16, represents a side view of the frame. As seen in Table 6, all of the parameters are included in the sketch of the frame, with the addition of two parameters on the head tube. The additional parameters define where the top and down tubes contact the head tube, as well as length of the head tube above the top tube. Since these parameters were not given by the sponsor they had to be obtained by physically measuring the frame where the top tube and down tube mate to the head tube.

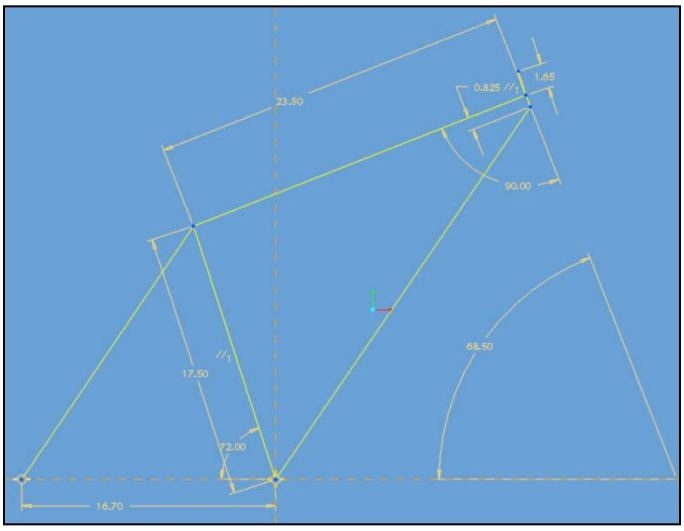

Figure 16: ProEngineer sketch of solid model geometry.

After creating the geometry, the eight individual tubes were created. The creation of each of the tubes can be seen in the following sections.

Down Tube

The down tube of the donated frames features a complex geometry including both a variable cross section and wall thickness. As seen in Figure 17, the down tube was sectioned into 10 total pieces to accurately model the tube. Vernier calipers were used to take measurements of the cross section and wall thickness of the 10 different sections.

Figure 17: Sectioning of the down tube for cross section measurements.

Table 7 summarizes the measurements taken from the frame. There were several sections of the frame that had a linear change in dimension, allowing for 4 total modeling sections to be used. The 4 sections consisted of a sweep with a uniform wall thickness, an extrusion with a variable wall thickness, another sweep with a uniform wall thickness, and finally an extrusion with a variable wall thickness.

Table 7: Data obtained from sectioning down tube

Distance from Head Tube (cm)	Thickness (cm)	Overall Height (cm)	Max. Width (cm)	
0	.29	5.08	4.06	Sweep
10.2	.29	4.75	4.25	Extrude
20.3	.15	4.75	4.25	Sweep
45.7	.15	4.01	5.74	Extrude
64.9	.10	4.01	5.74	

The 4 sections of the frame defined by the dimensions in Table 7 can be seen in Figure 18. As seen in the figure, the cross sections were defined at each of the specified distances, and the cross sections were swept in-between.

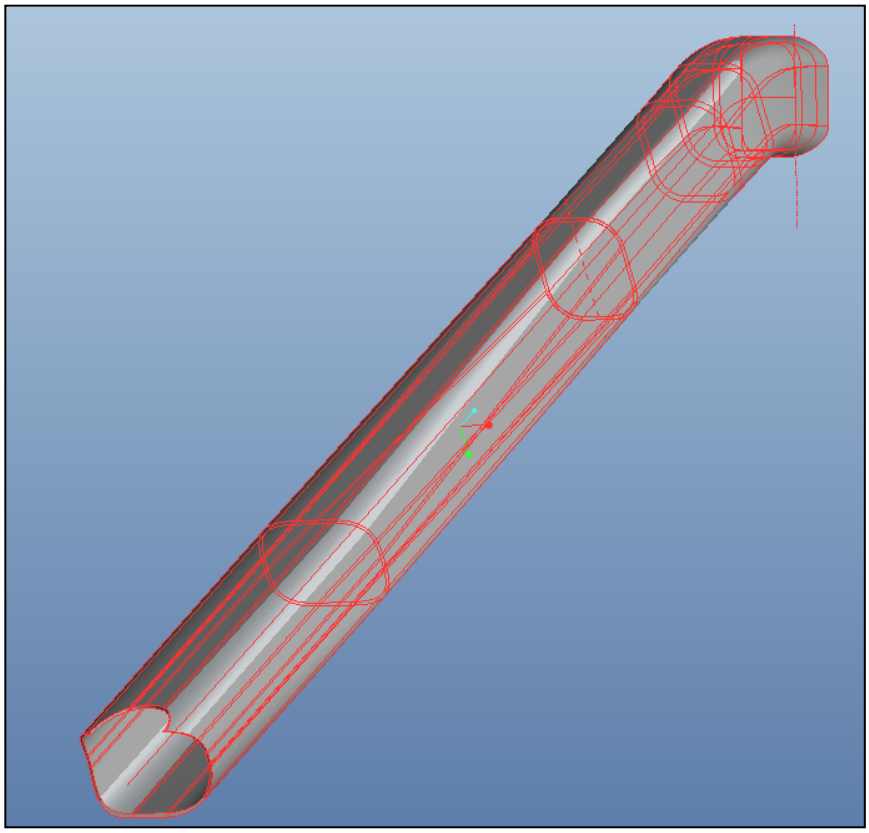

Figure 18: Solid model of down tube with accurate geometry.

Top Tube

The top tube also featured a complex geometry with variable cross sections. Similar to the down tube, the top tube was cut into 9 sections to analyze the cross section dimensional characteristics. The sectioned top tube can be seen in Figure 19.

Figure 19: Sectioned top tube for cross section measurements.

Once dimensions were taken from the frame sections they were plotted. As shown in Figure 20 the top tube dimensions change linearly, allowing for a simple swept blend to be used to model the tube. The correlation coefficients, as seen in Figure 20, were close to 1 which justifies the decision to use swept blend with linear dimension change.

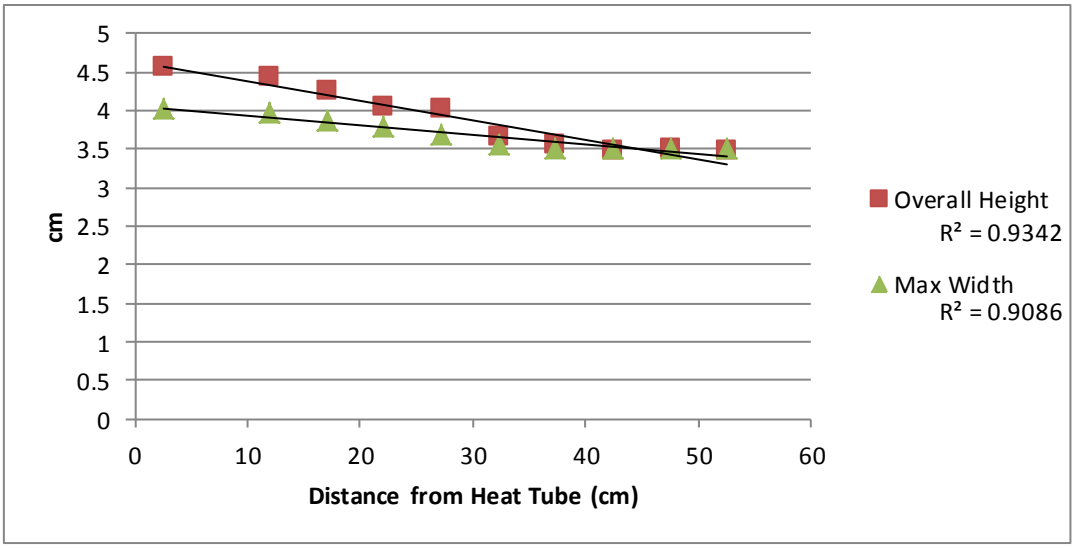

Figure 20: Top tube dimensional data from sectioning.

Rear Triangle Tubes

When modeling the rear triangle tubes, less consideration was put into their accuracy since they have simple geometries and minimal effect on the fatigue life of the frame. This modeling strategy can be seen in Table 8.

Table 8: Solid modeling strategy for rear triangle tubes

Frame Tubing	Modeling Technique Used	Notes
Seat stays	Sweeps	• Approximate model of the path of the swept section was used
Chain stays	Blended sweeps	• Thicker cross sections near the bottom bracket • Cross sections involved rectangular shape with filleted corners
Seat Tube and Bottom Bracket	Extruded circles	• Simple tubes
Dropouts	Extrude	• Simplified version of actual dropouts • Identical and mirrored on each side • Allowed for secure mounting during FEA

Tube Assembly and Mitering

The created tubes were then assembled together over the frame geometry sketch. The tubes were fixed to the appropriate locations based on the geometry sketch. For example, the bottom end of the seat tube was fixed at the connection point to the down tube. Once all the tubes were assembled, they were miter cut so that they did not intersect through the tubes they were mated with. A solid model of a miter cut tube can be seen in Figure 21. This process mimics how frames are actually manufactured. The mitering was accomplished by copying the geometry from the mated tube, then using this geometry to cut the correct portion of the mitered tube.

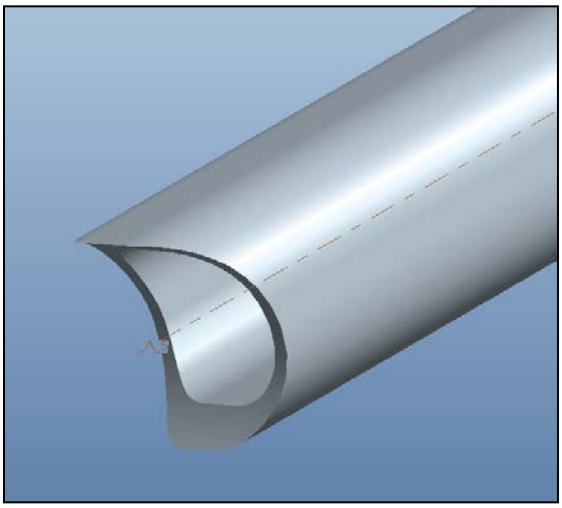

Figure 21: Example of a solid model mitered tube.

Accurate Material Properties

After the solid model was assembled, material properties were taken off of the donated frames, with specific focus on the material properties of the weld areas. The weld areas on the tubes were divided into three zones. These zones represented the weld,

the HAZ, and the unaffected parent material. By dividing the tube into these three zones, different properties were able to be applied to each area.

The sizing of the three different zones was determined by taking Rockwell hardness measurements on samples from each respective zone. Once the samples had been prepared, they were tested on a Rockwell indenter using the Rockwell E scale (HRE). The HRE utilizes a 1/8" diameter ball to indent the material with a minor load of 10kg and major load of 100 kg. By doing this test, the hardness values of the material moving away from the weld were determined. Using this information, the zone sizes were established to best represent the changing properties.

The HRE scale was chosen specifically for this application due to the ability to correlate hardness values to ultimate tensile strength (UTS). In this case, a simple equation $UTS = 10.66 - 19.42 * \ln(1 - \frac{HRE}{109})$ was used to derive the variation in UTS across each zone [49]. Figure 22 shows the variation in UTS.

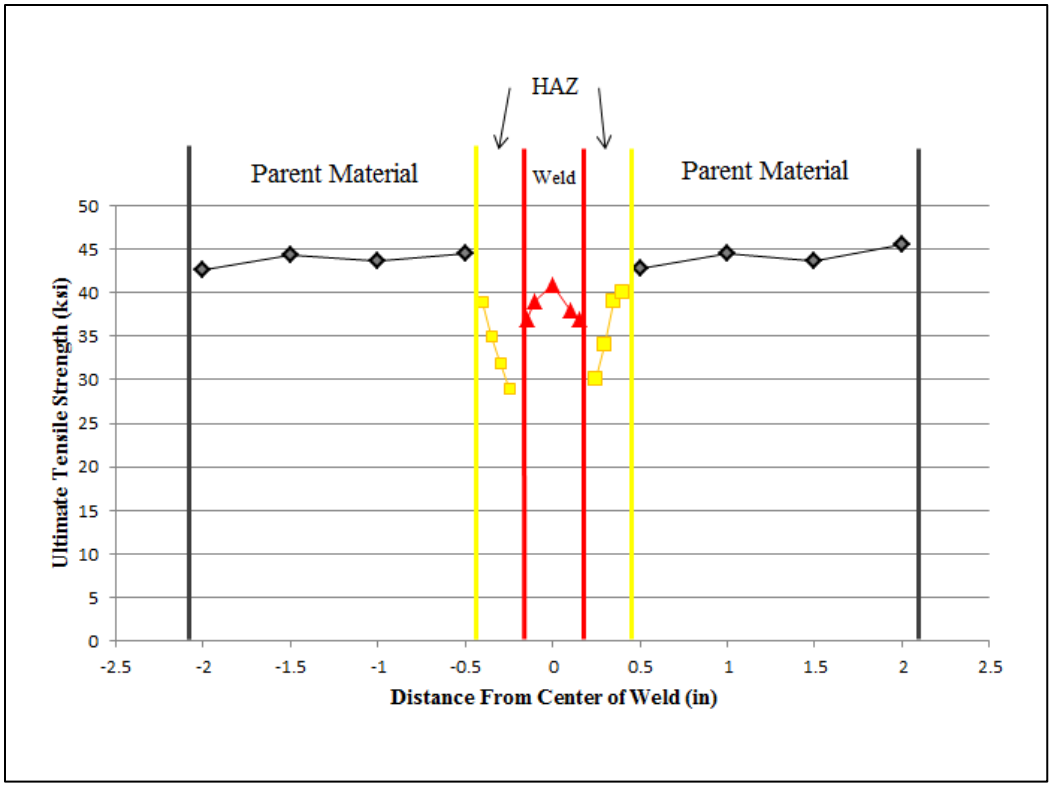

Figure 22: UTS measurements obtained from Rockwell hardness test.

Once these measurements were completed, the average UTS for each zone was calculated and inputted into the solid model to complete the modeling of the three zones. The final data used to model each zone is shown in Table 9.

Table 9: UTS summary for different weld regions

	Weld	HAZ	Parent Material
UTS (MPa)	289.7	239.3	307.6
Length (cm)	0.95	0.63	Part length

As can be seen in the previous table, the parent material and weld exhibited a higher UTS than the HAZ. This result was expected, as the ASM Handbook defines a similar variation in UTS across a 6061-T6 weldment as seen in Appendix E.

The data for the HAZ and weld sizing was used to modify the solid model to include these areas. Figure 23 shows the front triangle area with the weld zones marked. The red color represents the weld, the yellow represents the HAZ, and the grey represents the parent material.

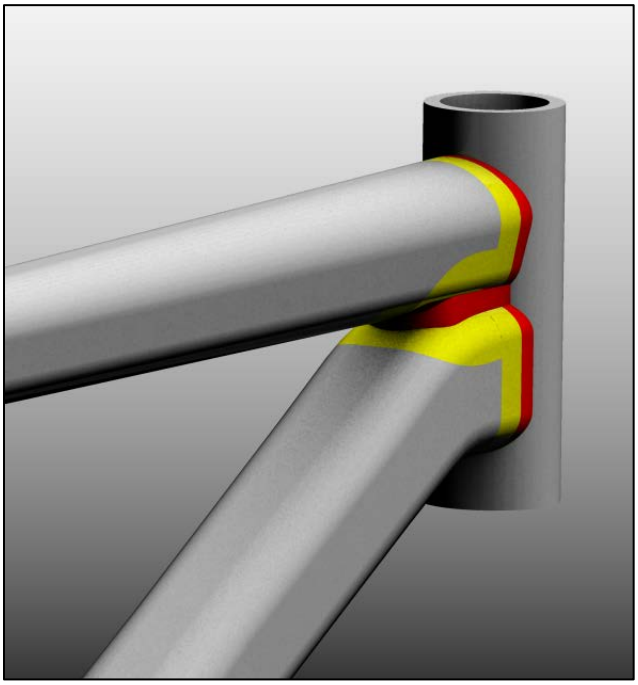

Figure 23: Solid model showing TIG welding zones.

The entire frame solid model can be seen in Figure 24. This includes all of the assembled tubes and the weld zones.

Figure 24: Completed solid model of physical frame.

Test Fork Solid Model

A test fork solid model was created based on the ASTM F2711-08 test requirements to allow for the FEA to be conducted. The test standard defines two parameters for the fork, length of the fork, and rake of the front dropout connection. The design of the test fork was representative of the design of a fork manufactured by the group for testing discussed in Section 3.3.1.

3.2.2 FEA

Once the solid model of the donated frame and the test fork were created, an FEA was conducted with ANSYS Workbench 13.0 using the solid model. An FEA is a computer based numerical method which models an object with a mesh of separate elements connected by nodes to determine stress, strain and a number of other properties

[14]. The decision was made to use ANSYS Workbench 13.0 due to its ability to import solid models created in ProEngineer, and the software's ability to simulate fatigue loading on the frame. The procedure for setting up the model in ANSYS is described in the following sections.

Localized Meshing Control

Meshing for the model was done using the automated meshing refinement feature in ANSYS and can be seen in Figure 25. Added resolution was used for the head tube, weld zones, and upper top and down tubes. This added resolution decreased the element size, and increased the total number of elements in these areas. This allowed for more accurate understanding of the behavior in this area since this area is predicted to fatigue fail based on the frame recall information discussed in Chapter 1. Larger element sizes were used in the rear triangle of the frame, and in the fork due to the reduced need for these areas to be accurate since these areas were predicted to fail with higher loads and higher cycles.

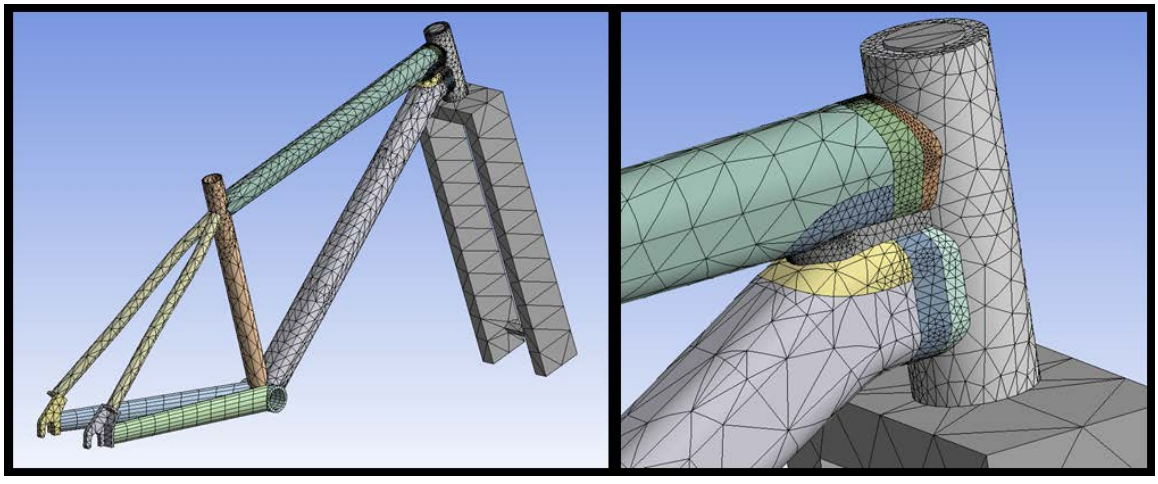

Figure 25: Solid model of bike frame after applying the mesh.

Boundary Conditions and Loading

Following the ASTM F2711-08 test standard, boundary conditions and loads were applied to the frame in ANSYS Workbench 13.0. A force of 1,200 N was applied to the test fork so that the force was parallel to the rear dropouts. The force was applied in the direction away from the rear dropouts as defined by the ASTM F2711-08 standard. Since tensile stress is the cause of fatigue failures the group decided to model the 1,200 N tensile force for analysis. Boundary conditions were then applied to the rear dropouts as fixed support conditions as defined by the ASTM F2711-08 test standard.

FEA Output Model

The group investigated areas on the frame with high levels of tensile strain to predict where the failure on the frame would occur. This was done by generating result outputs for the model showing tensile stress levels. The analysis was based on the fact that areas with high levels of tensile stress produce high levels of tensile strain, and thus produce fatigue failures. The output from ANSYS can be seen below in Figure 26.

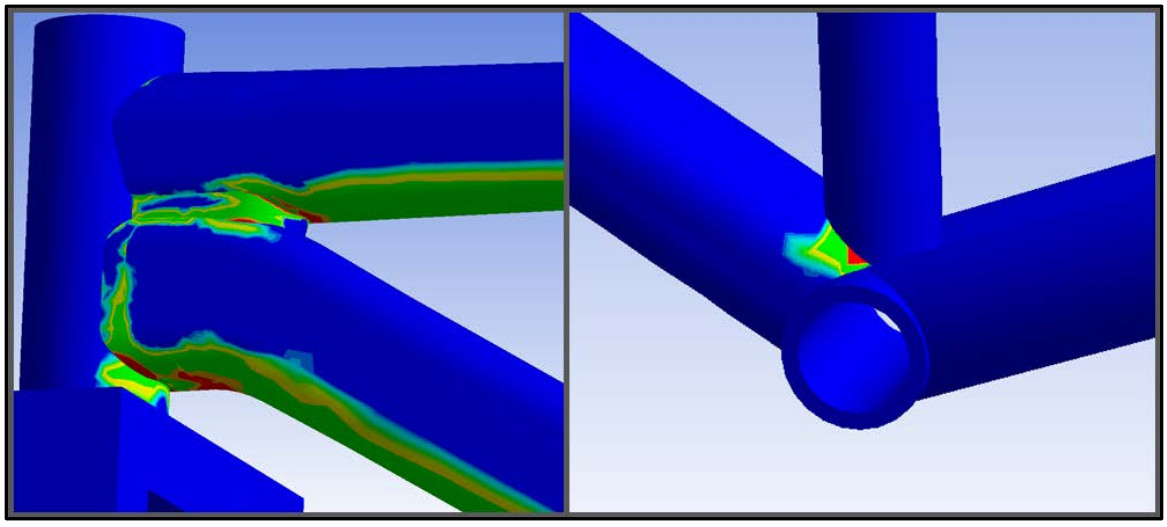

Figure 26: FEA output showing tensile stress and correlation to fatigue failure location.

Based on the FEA output, there were three main areas on the bicycle frame with a susceptibility to fatigue failure. These areas were the top tube near the weld to the down tube, on the down tube near the weld to the seat tube, and on the down tube near the weld to the head tube. Based on the grain structure of the top tube and down tube discussed in Chapter 2.2.1, the group decided that the down tube tensile and fatigue strength would be higher than the top tube, especially near the head tube due to the small grain size. Small grains generally correlate to higher fatigue strength [27]. Due to this, the predicted fatigue failure locations include the top tube near the weld to the down tube, and the down tube near the weld to the seat tube.

The group worked to then calculate the predicted number of cycles before failure in these two locations. This was done by determining stress levels in the areas likely to produce fatigue failure and use these levels to determine cycles to failure from S-N curves. The stress levels for these areas were taken from an output in ANSYS showing von Mises stress since ANSYS does not have an output showing only tensile stress. This output can be seen in Figure 27. From the solution output, the stresses in these areas were calculated to be approximately 95 MPa for the three areas of predicted fatigue failure.

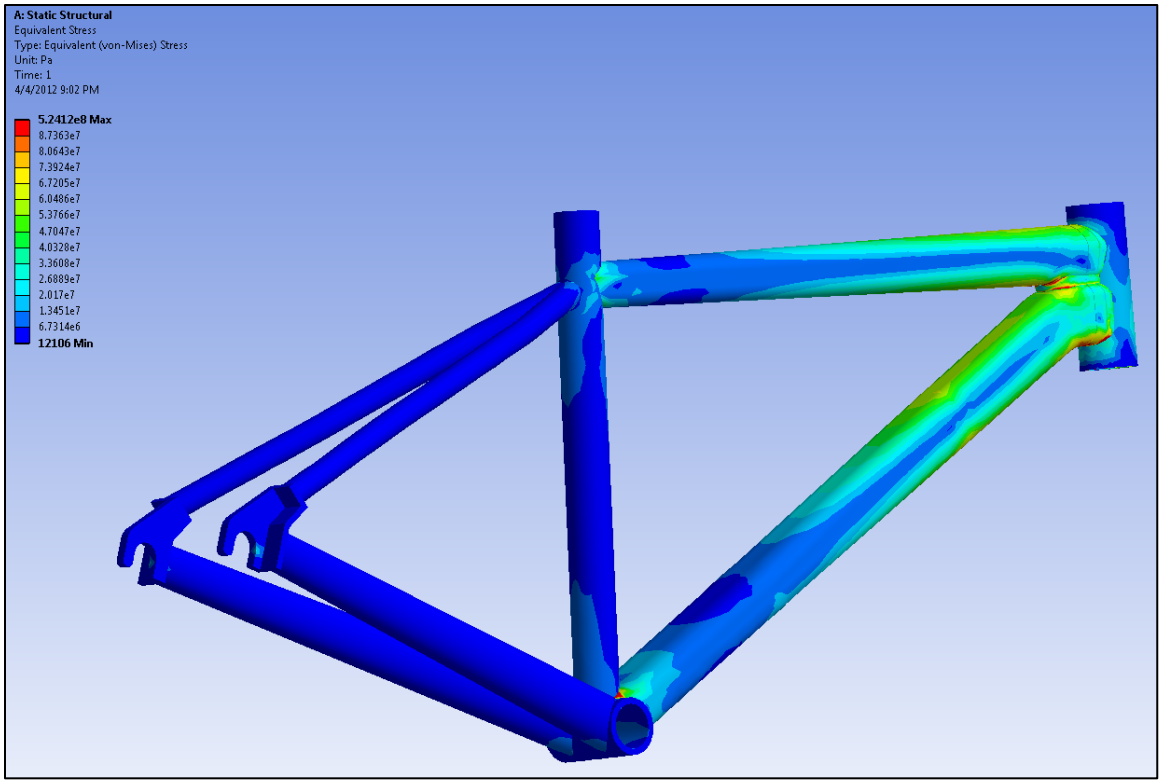

Figure 27: FEA output of entire frame showing von Mises stress.

The group used the von Mises stresses in the areas of high tensile stress to determine the cycles to failure. A 6061-T6 S-N curve with a stress ratio (R) value of -0.5 was used to correlate the stress levels to cycles to failure. The R value was calculated below based on the loading defined by the ASTM F2711 test standard.

$$Stress\ Ratio\ (R) = \frac{Stress_{min}}{Stress_{max}} = \frac{-600}{1200} = -0.5$$

Since the S-N curve provided a wide range of cycles to failure for a given stress, the group decided to create a line in the range that represents the predicted level to failure. This can be seen in Figure 28. The line was made on the conservative side of the center of the range, and was compared with other S-N curves for 6061-T6.

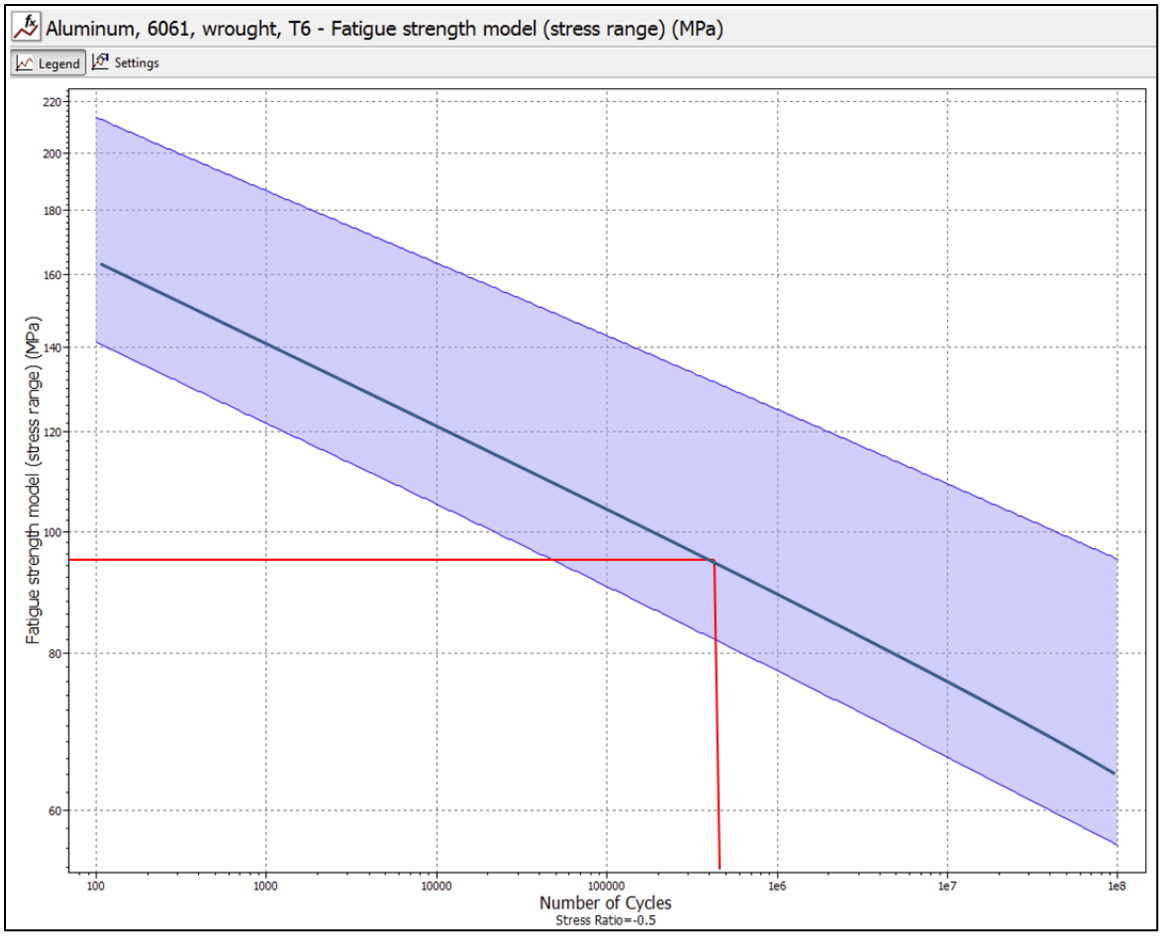

Figure 28: Aluminum 6061-T6 S-N curve showing predicted failure at 490,000 cycles.

From the S-N curve, the group concluded that the predicted cycles to failure for the bicycle frame was 490,000 cycles on the top tube near the weld with the down tube, and on the down tube near the weld to the seat tube.

3.3 Frame Testing

Physical fatigue tests were conducted on the donated frames to validate the integrated FEA methodology. These physical tests followed the ASTM F2711-08

horizontal fatigue test standard, and allowed for validation of the FEA results. The group worked to develop a test rig, tested the frames, and observed fatigue failures on the frames.

In order to conduct the horizontal fatigue test outlined in the ASTM F2711-08 test standard, an adequate testing rig first had to be constructed. The group created the test rig by designing and creating a test rig structure, and control system for the rig.

3.3.1 Test Rig Structure Development

The test rig structure had to meet a number of specifications as defined by the ASTM F2711-08 test standard. These specifications can be seen below.

Test Rig Structure Specifications

- Securely hold the rear dropouts of the bike frame
- Securely hold the head tube of the frame to a test fork
- Include a rigid test fork that will not deflect with up to 1500 N of force
- Hold the rear dropouts and test fork mount at the same height
- Apply a force of 1500 N on a test fork in the positive direction (away from the rear dropouts)
- Apply a force of 750 N on a test fork in the negative direction (towards the rear dropouts)
- Run for at least 500,000 cycles
- Be able to be mounted on a 5’ by 2.5’ desk

The group designed the test rig to meet the specifications above. The design created by the group involved a test rig frame, air cylinder, dropout holders and a test

fork. These components can be seen in Figure 29, and the specific design and fabrication of each of these elements is described in the following paragraphs.

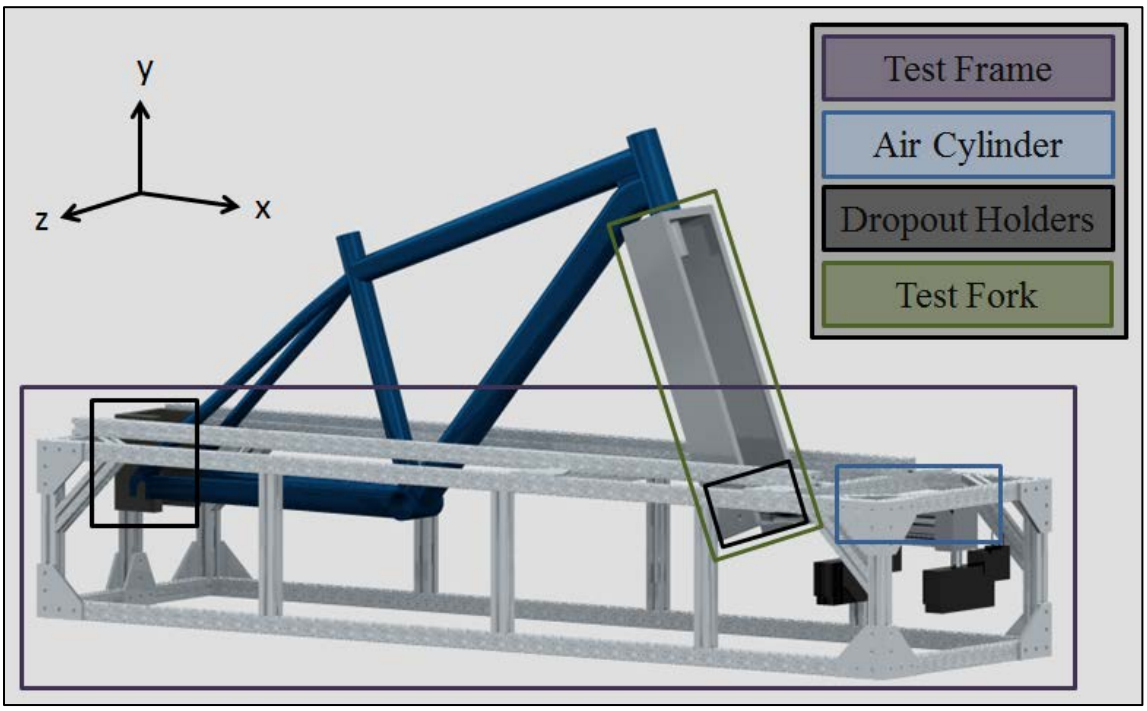

Figure 29: Structural components of test rig.

Test Rig Frame

A test rig frame was chosen as the first part of the test structure to design and fabricate. The test rig frame was designed to be the supporting structure for which the other structural components were mounted. The bicycle frame was then horizontally mounted to these components. T-slotted extrusions from 80/20 were chosen to use for the rig support structure. This decision was based on the extrusions' adequate material properties, ease of assembly, and vibration proof connections. Made of 6105-T5 aluminum, 80/20 is a modular industrial erector set, allowing for easy assembly. The 6105-T5 aluminum 80/20 extrusions were predicted to have adequate stiffness (82 GPa)

to support testing. The connections utilize a 2 degree drop lock, which makes the connections vibration proof, which is favorable based on the prediction of high vibrations during testing [1].

Figure 30 shows the solid model and physical structure of the 80/20 test frame. As seen in the figure, the design incorporates a box-like structure, with supports running in the vertical, longitudinal, and latitudinal directions. These supports add to the stiffness of the test frame, making it adequate for fatigue testing. The test rig length was designed to encompass the entire bicycle frame as well as the other components of the test rig. The final dimensions of the test frame were 42 cm wide and 1.47 m long which met the size specification defined by the group.

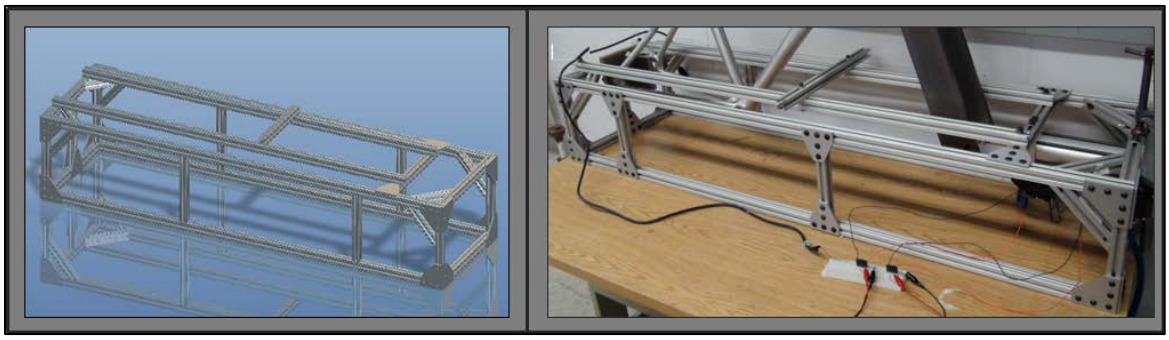

Figure 30: Solid model and fabricated 80/20 test rig frame.

Air Cylinder

A double acting single ended air cylinder was used to exert 1,200 N retraction and 600 N extension forces for testing. A 2" bore air cylinder with ¼ NPT fittings was chosen for the task as it is capable of producing 1,200 N of force at exactly .62 MPa (90 psi), as seen in Appendix D. The shop air accessible to the group had a maximum pressure of .83 MPa (120 psi) allowing for pressure drops of up to .21 MPa (30 psi)

before the compressor would be unable to provide the necessary pressure. This ensured the air cylinder would always have enough air pressure to transmit the correct load even when other machines were using air from the compressor. The air cylinder extends when pressure is fed into the back section, and retracts when air is pumped into the front section. The air cylinder is shown in Figure 31.

Four quarter inch mounting holes were drilled into two of the cross beams on the 80/20 test frame to mount the air cylinder to the test rig. These holes matched up with the mounting holes provided on the air cylinder, allowing for it to be bolted directly to the support structure.

Figure 31: Air cylinder used to exert forces onto tested bike frame.

Dropout Holders

Two of the most crucial components of the test rig were the front and rear dropout holders. These holders act as the connection from the test rig to the bicycle frame, and must be secure enough to allow for proper fatigue loading of the donated frame. Per the ASTM F2711-08 standard, there are only two specifications for the bicycle frame dropouts: they must be securely held, and must also be horizontally aligned with the

force. This concept is illustrated in Section 2.6.1. The rear dropouts were secured to a plate which was then bolted to the end of the rig opposite the air cylinder. Additional 80/20 extrusions and bolts were used in securing this section to ensure its stability. This setup can be seen in Figure 32.

Figure 32: Rear dropout base plate fixtured to test rig frame.

The rear dropout holder is constructed and mounted in a way that accomplishes two important tasks. First, by placing all of the bolts for the dropout holder in axial tension and compression, the assembly becomes much stronger. This is because bolts are designed to be loaded axially and not in shear. The second important aspect is that the rear dropout holder is mounted in such a way that there is no unsupported moment during loading. Again, this ensures that the test rig structure is as solid as possible, and that the loads from the air cylinder will be properly transmitted to the bicycle frame.

Steel bar stock was chosen to use to manufacture the dropouts to ensure that they would not fail or deflect during operation of the test rig. Manufacturing the dropout

holders consisted of drilling and tapping two mounting holes into the back of the plates to secure them to the back plate. Next the mounting holes for attaching the rear of the bicycle frame to the dropout holders were drilled. After the rear dropout holders were created, the mounting plate that connects them to the test rig itself needed to be fabricated. This was completed by acquiring a bronze base plate and drilling seven holes into it: four holes to mount the rear dropouts, and as three additional holes to mount the base plate to the test rig. An exploded view of this assembly can be seen in Figure 33.

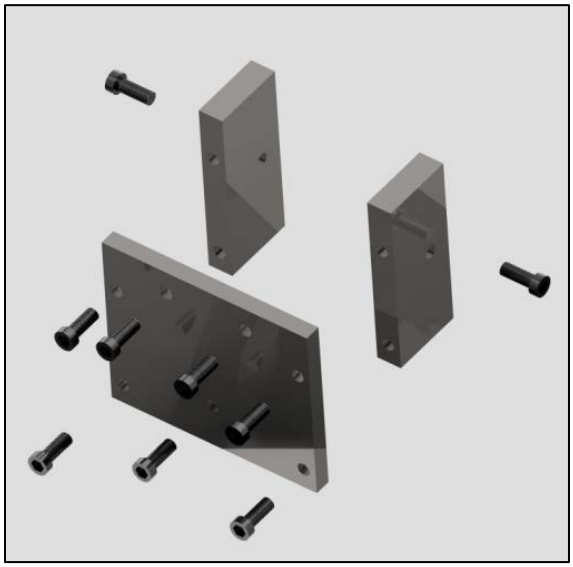

Figure 33: Exploded view of rear dropout assembly.

The front dropout was created from a length of square cross-section aluminum. The piece was first cut to length on the band saw, and then the mini-mill was used to cut and tap the two mounting holes that would attach it to the test fork. A third and final hole was then drilled and tapped in the center to connect the dropout to the air cylinder's piston. This allowed the group to utilize the threaded rod attached to the piston, and further simplified the fabrication process. The decision to use aluminum was based on

ease of manufacturing to make the center hole, and was of adequate strength due to the large cross sectional area. This setup can be seen in Figure 34.

Figure 34: Threaded rod of air cylinder screwed into front dropout.

Test Fork

Attached to the front dropout holder was a test fork, which was designed and manufactured based on the ASTM F2711-08 standard. The design of the test fork is composed of two plate arms with a plate cross member and tube running through the cross member. The test fork served as the main link between the air cylinder and the bicycle frame, and needed to be strong enough to ensure that all of the force was transmitted into the frame. Steel was the material of choice because it has a much higher modulus of elasticity (205 GPa) when compared to 6061 (72 GPa) as discussed in Chapter 2. With a higher modulus of elasticity, the steel required much more force to deflect compared to the aluminum frame.

The group manufactured the test fork using a lathe, overhead mill, and band saw. The steerer tube was turned using the lathe to 2.86 cm in diameter. A close fit hole for the steerer tube was cut through the cross member using an overhead mill. The test fork arms and cross member were cut from a 1.27 cm thick plate using a band saw. The test fork arms were welded onto the cross member, and the steerer tube was welded into the hole of the cross member. A standard 1 1/8 inch headset was used for mounting the fork to the frame. The solid model of the test fork along with the completed test fork can be seen in Figure 35.

Figure 35: Solid model of test fork and fabricated test fork.

3.3.2 Test Rig Controls Development

While designing and manufacturing the structure of the test rig, the group concurrently designed the control system. The control system needed to meet a number of specifications to be able to perform the test following the ASTM F2711-08 standard. The group defined the specifications required to control the rig as follows:

Test Rig Controls Specifications

- Direct .83 MPa (120 psi) of air pressure into the air cylinder for tensile loading
- Direct .41 MPa (60 psi) of air pressure into the air cylinder for compression loading
- Cycle air loads at 1 Hz
- Run for at least 500,000 cycles
- Run using resources available in HL-031 Laboratory

The group worked to accomplish the task specifications and came up with the design described below. The group decided that the system would consist of 2 solenoids, 2 pressure regulators, and an electrical circuit that would be controlled using a LabVIEW Virtual Instrument (VI).

The entire control system for the test rig can be seen in Figure 36. As seen in the figure, the orange boxes represent the electrical circuit, with a DC input signal from LabVIEW, which control the solenoids. The solenoid valves allow air from the air compressor, regulated using pressure regulators, into the double acting pneumatic cylinder. Each of the components of the control system are discussed below Figure 36.

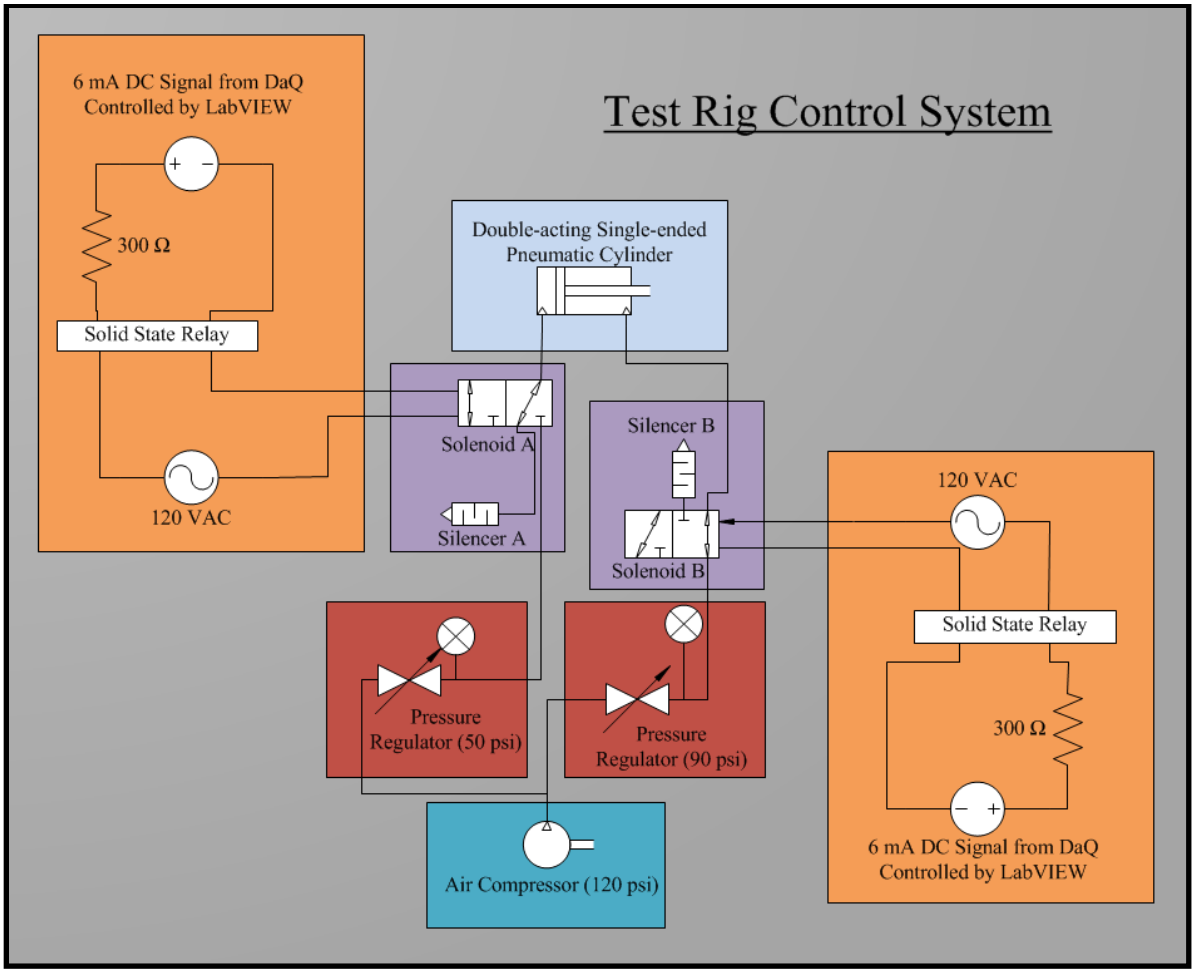

Figure 36: Operation diagram for test rig control system.

Solenoids

Solenoids were chosen to control the air cylinder due to their ability to channel air flows using a supplied voltage. Two 3-Way, 2-position, 120 VAC solenoids were chosen for the test rig control system. By using two solenoid valves, the ports of the air cylinder were able to be controlled independently. The 3-way, 2 position solenoids were chosen so that the air would be able to enter through a designated port and then, depending on whether or not the solenoid was powered, either pass the air into the air cylinder or hold it in the valve itself. The two air flow paths for the solenoids can be seen in Figure 37. As

seen in the figure, the air can travel through the solenoid when powered, and exhaust through the solenoid when not powered.

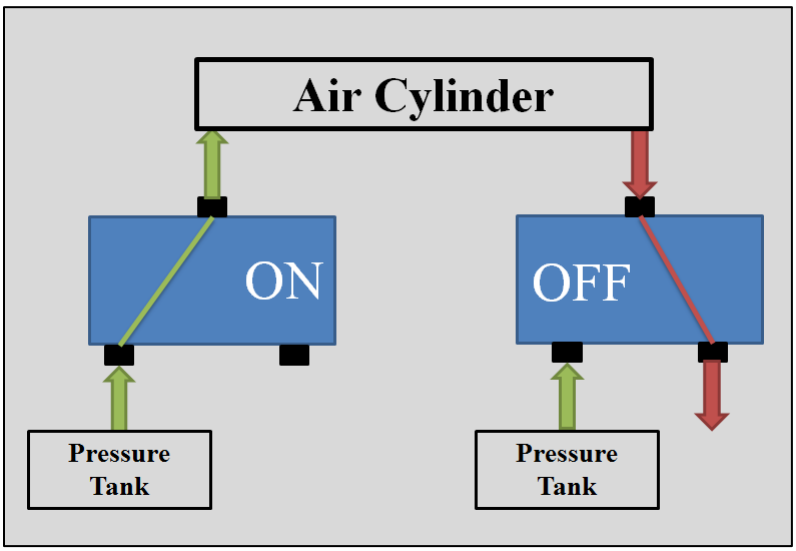

Figure 37: Solenoid air flow path diagram.

Solenoid valves powered by 120 VAC were chosen so that they could be powered using a common wall outlet. The solenoids used on the test rig can be seen in Figure 38. As seen, the solenoid is mounted directly to the bottom of the air cylinder.

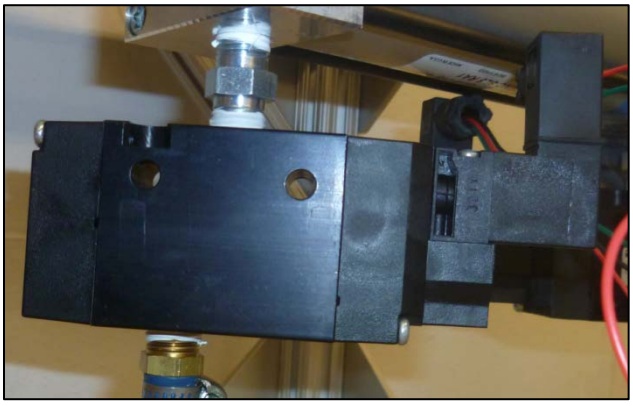

Figure 38: Solenoid valve connected to air cylinder.

Mufflers were used on the solenoids to reduce the noise of the test rig during testing. The mufflers were made from sintered bronze and still allowed for adequate airflow to ensure proper air escape from the solenoid.

Pressure Regulators

Pressure regulators were used to control the air pressure flowing to the solenoids. The chosen air cylinder had a chart on the data sheet, as seen in Appendix D, which allowed for the pressures to be calculated, outputting the force required by the ASTM F2614-09 standard. Pressure regulators were chosen based on their ability to regulate a pressure range of .28-.86 MPa (40-125 psi).

Circuit – Solid State Relays

An electronic circuit was developed to allow for the solenoids to be controlled and powered. This fabricated circuit can be seen in Figure 39. The circuit schematic can be seen in Figure 36. The circuit utilized solid-state relays to allow a DC input signal to control a 120 VAC voltage. When a signal was sent to the solid-state relay, the relay would open and allow for the 120 VAC to pass through the circuit. A resistor was used to properly control the DC voltage input signal.

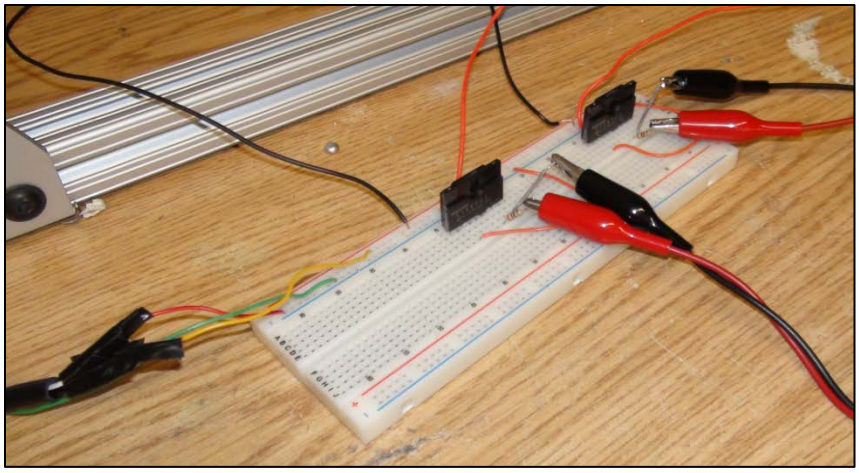

Figure 39: Circuit including SSRs to control solenoid valves.

LabVIEW

LabVIEW was utilized to control the circuit at the 1 Hz rate specified by the ASTM F2164-09 test standard. LabVIEW was chosen based on its simplicity of use for generating signals and recording data. The developed LabVIEW VI front panel can be seen in Figure 40. The panel works by allowing the group to choose the output voltages going to each solenoid, the delay time or speed of movement, and includes a count of the cycles completed. When the VI is operating, a 5V signal is sent to two TRIACS in the control system circuit in an alternating fashion.

The simple VI created to output the alternating voltages works by way of a shift register, and an if/then logic sequence. The shift register and if/then sequence with a time delay allow for the circuit to output 5V to one TRIAC for .5s, then switch to a 5V output to the other TRIAC for .5s. The back panel of the VI can be seen in Appendix B which shows the logic of how the VI works.

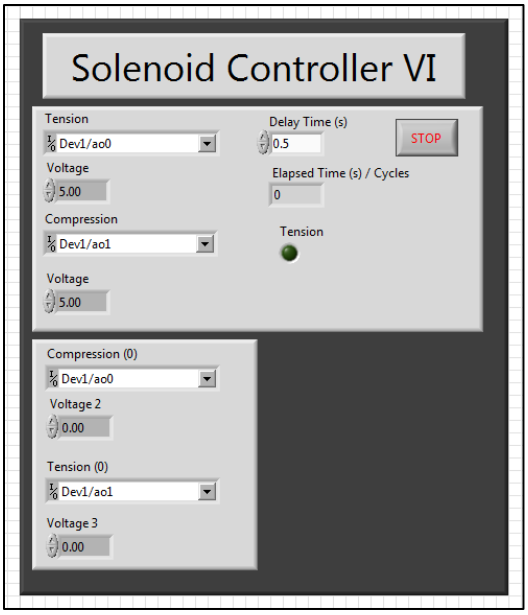

Figure 40: Solenoid controller front panel developed in LabVIEW.

3.3.3 Complete Testing System

The actual testing rig can be seen in Figure 41. As shown on the right, the computer is used to control the entire test rig through the DaQ and circuit. On the left side of the figure the test rig structure is shown with the donated frame mounted on it using the practices discussed previously. After the test rig was ready to perform the task specifications, the group created a procedure that would allow for the most accurate results, and allow multiple tests to be conducted the same way.

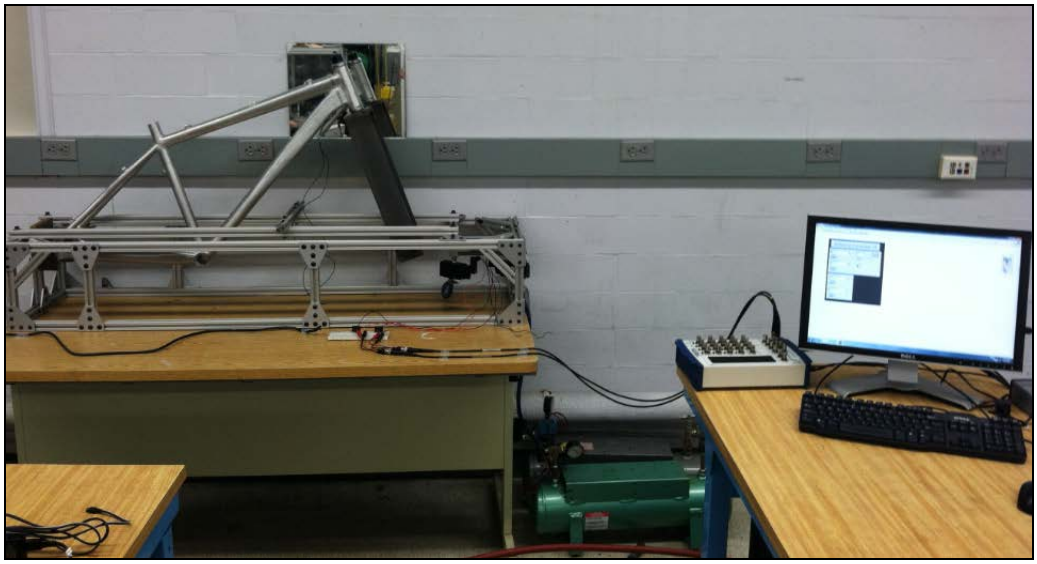

Figure 41: Testing rig with structure and controls.

3.3.4 Testing Procedure

With the test rig completed, the group developed a comprehensive testing procedure to ensure accurate results with the test. The procedure for conducting the tests can be seen below.

Setup

1. Ensure that all bolts and screws are tightened on the test rig
2. Fixture test rig to table using C-clamps
3. Connect the front dropout holder to the threaded rod on the air cylinder
4. Place rear dropouts on dropout holders and tighten skewers
5. Ensure that frame is sitting level on the test rig
6. Connect solenoid valves to air cylinder ports
7. Connect tubes running from solenoid valves to pressure regulators
8. Connect pressure regulators to pressure accumulators

9. Connect shop air to each pressure tank
10. Using pressure regulators adjust air pressure to desired amount
    a. For this application, the necessary pressures are .34 MPa (50 psi) to the back port and .62 MPa (90 psi) to the front port
11. Setup high definition video camera level with front triangle connection (emphasis on top tube / down tube weld zone)

Testing

12. Run test for 10 cycles while taking strain measurements (described in next section)
13. Ensure that test rig is creating proper strain levels on the frame
14. Begin recording video
15. Begin applying load at 1 Hz (Ensure LabVIEW file is set to Time T=0)
16. Visually inspect frame for first 3,000 cycles
17. Visually inspect frame after 50,000 cycles (observe/take notes during crack growth, record initial crack through propagation)
18. Conclude test when fracture occurs (Fracture is a crack, tear, or separation at the surface of the frame that is visible to the unaided eye)

3.3.5 Test Rig Performance Investigation

In order to determine whether the test rig was working correctly, a strain gage was used to monitor the strain of a section of the bicycle frame. The recorded strain was then compared to the FEA to ensure that the proper strain levels were being achieved.

In order to determine the strain of the frame during testing, a strain gage was attached to the frame on a flat area which the FEA indicated would have high levels of strain during the test. This area was determined using a FEA of strain under loading. The FEA solution can be seen in Figure 27. Based on the solution, the group chose to

place a strain gage on the bottom of the down tube with expectations of strain in the range of 800-1,200 microstrains (strain expressed in parts per million).

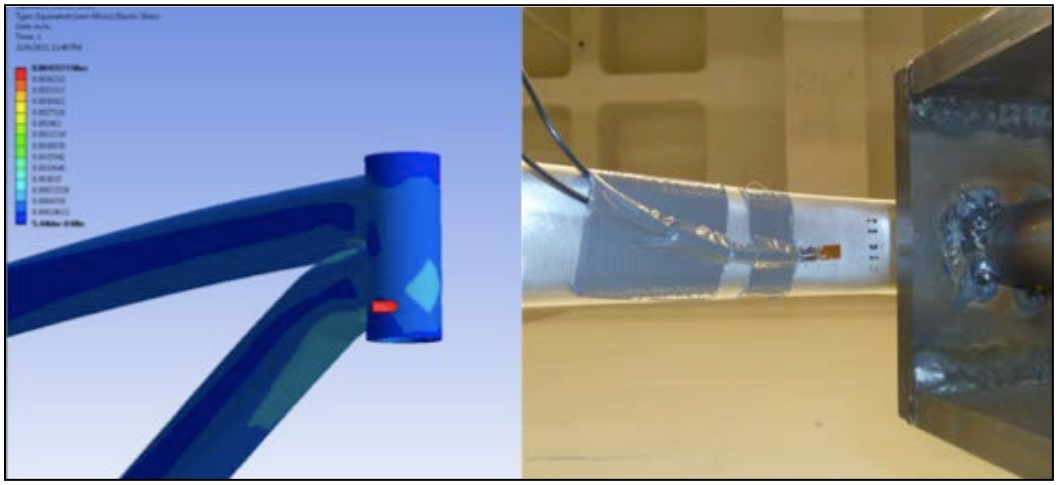

Figure 42: FEA strain levels (left) and strain gage placement (right).

A strain gage was attached to the frame on the underside of the down tube as seen in Figure 42. In order to monitor the strain, the group chose to use a LabVIEW VI as well as a Wheatstone bridge. This decision was made based on the ease of developing a VI to record the strain from the strain gage.

A Wheatstone bridge was chosen to monitor the small change in resistance of the strain gage to determine the strain during the test. Without the use of the Wheatstone bridge no change in resistance would be perceivable, as it allows for accurate recording of small resistance changes. The schematic for the Wheatstone bridge used can be seen in Figure 43. The strain gage attached to the frame functions as resistor 4 (R4) in the schematic, and when the resistance changes as the gage is flexed, the voltage between nodes A and C is measured and the resulting strain can then be calculated.

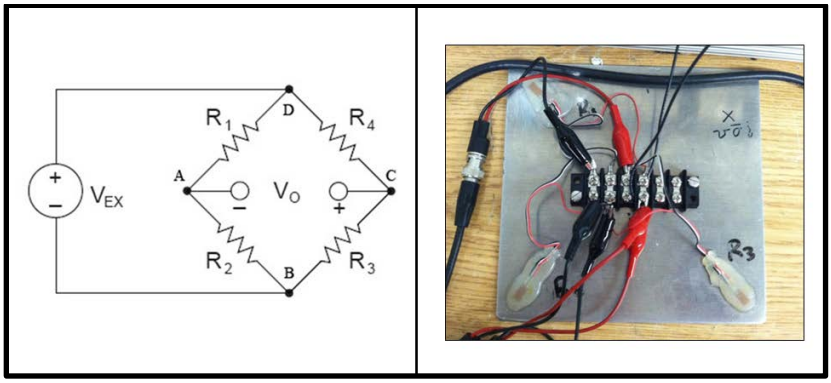

Figure 43: Wheatstone bridge schematic (left) and physical layout (right).

The physical Wheatstone bridge circuit can be seen in Figure 43. An input voltage with cables monitoring the voltage is attached to the circuit, as well as cables measuring the voltage between nodes A and C.

LabVIEW was chosen as the software to monitor and record the strain of the frame. The front panel of the VI can be seen in Figure 44. The front panel allowed the group to be able to set the output channels, the delay time for recording, a voltage output to the strain gage, data for the strain gage, and to perform a calibration by simulating strain using shunt resistors. Once the data was recorded for each shunt resistor, these values were compared to the calculated strain for each change in resistance, and a slope and intercept calibration was developed.

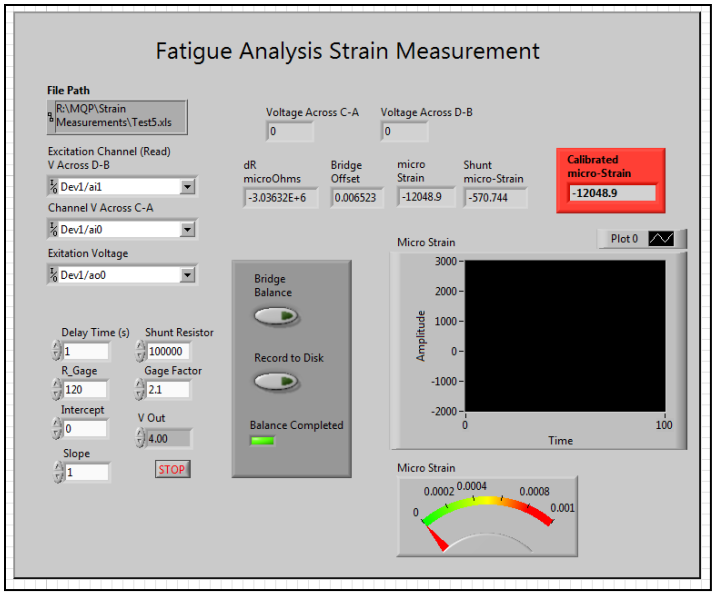

Figure 44: Strain measurement front panel developed in LabVIEW.

The LabVIEW back panel can be seen in Appendix C. The back panel shows the wiring and programming behind the VI. The group ran the test rig for ten cycles while taking strain measurements. The bridge was balanced and data was recorded during the test. The strain during the application of 1,200 N was found to be ~1,000 microstrains. This value was within the FEA prediction (800-1,200 microstrains). Due to the strain measurement being within the predicted value, the group determined the test rig was working appropriately and that it was ready for a full test until the mounted frame experienced a fatigue failure.

The force exerted from the air cylinder was measured using a force plate to verify the loading was 1,200 N. After the test rig performance investigation was completed, the remaining procedure steps were done to conduct the test. The results for the tests are described in the following section.

4.0 Frame Testing: Results, Comparison, and Analysis

4.1 Results and Comparison

Two bicycle frames were donated to the group, and both were physically fatigue tested. One frame was physically tested by the group using the test rig and methods described above, and the other was sent out to an external frame testing company. The external testing company was Engineering Materials Lab in California which specializes in fatigue testing. Testing at WPI and at an external facility allowed for validation of the group's physical testing rig.

The frame that was tested by the group failed on the top tube in the HAZ created from the weld to the down tube. The frame tested by the outside company failed on the down tube in the HAZ created from the weld to the bottom bracket. The two crack initiation locations can be seen in Figure 45 along with the FEA result output for predicted failure location. As seen in the figure, the failures occurred in two of the three zones predicted by the FEA for fatigue failure.

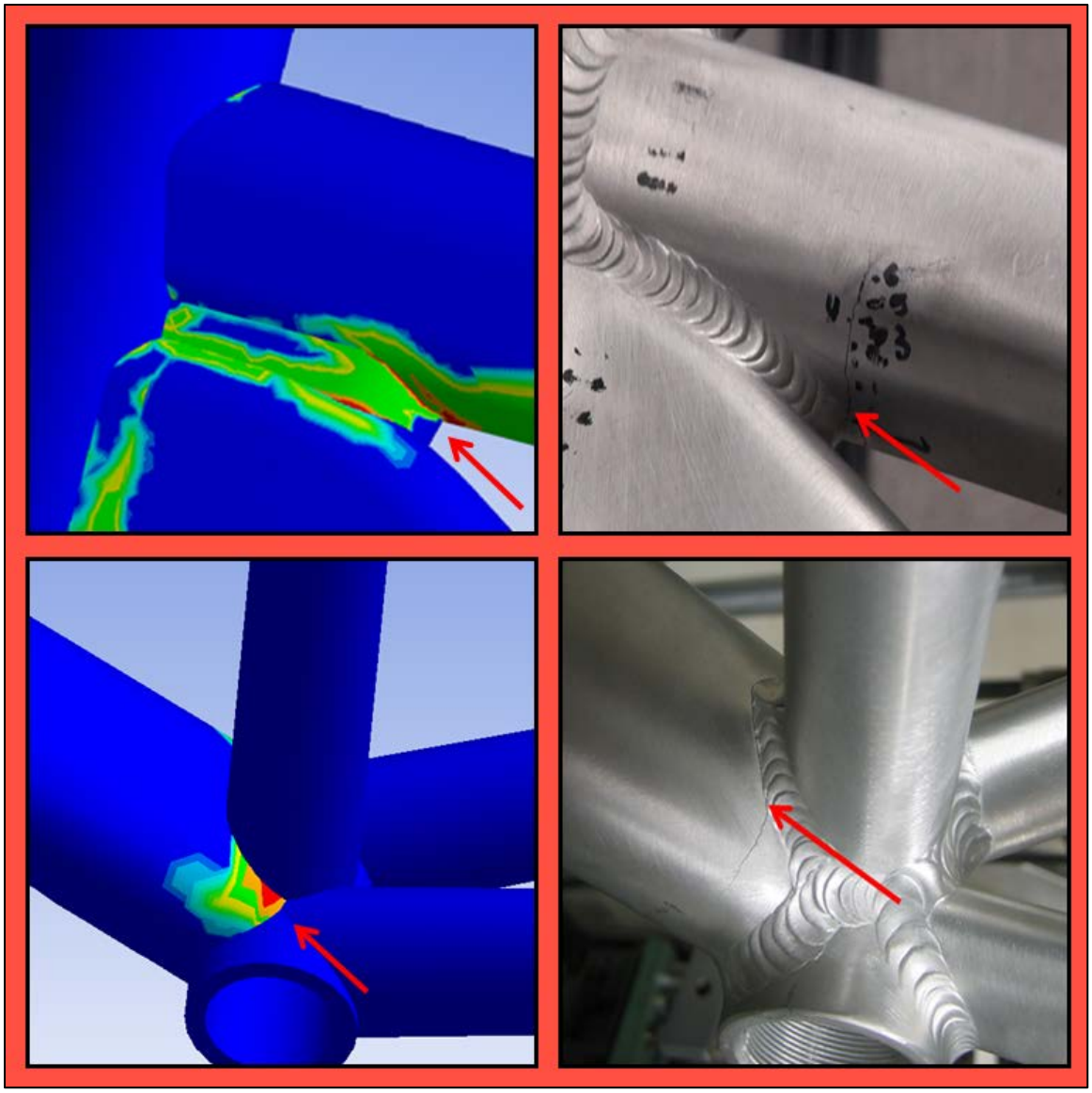

Figure 45: FEA (left) and tested (right) fatigue failure locations showing agreement.

4.1.1 Calculating Equivalent Cycles

Due to a misinterpretation of the test standard, and a modification to the test plan, the test rig was run with several different loading scenarios. The test rig was initially run with the loading reversed from the ASTM standard, which generated 600 N in tension

and 1,200 N in compression. Due to this error on the part of the group, the equivalent cycles were calculated to determine the cycles to failure with correct loading. Also, the group increased the loading after the frame passed the ASTM standard by a significant number of cycles. This was done to be able to produce a failure in a timelier manner.

The group calculated the equivalent cycles based on the Miner's rule. Miner's rule is summarized by the equation below. Miner's rule shows that it is possible to assess the proportion of cycles to failure for different stress levels in order to determine equivalent cycles to failure.

$$\sum_{i=1}^{k} \frac{n_i}{N_i} \approx 1.0$$

Based on this rule, the equivalent cycles to failure for the different loading scenarios were calculated below in Table 10. The cycles to failure adjusted for the HAZ was done based on the assumption that the cycles to failure for the HAZ was proportional to the cycles to failure just as the UTS for the HAZ is proportional to the UTS for 6061-T6.

Table 10: Equivalent cycles for physical frame testing

Loading (N)	Cycles at Load	Predicted Cycles to Failure at Load (FEA)	Predicted Cycles to Failure (Adjusted for HAZ)	Percent to Failure (%)	Equivalent Contribution Cycles to Failure (1,200 N)
600	311,883	10,000,000	7,000,000	4.50	21,832
1,200	344,893	700,000	490,000	70.40	344,893
1,500	23,550	200,000	140,000	16.80	82,425
				Total	449,150

As seen in Table 10 the total cycles to failure from physical testing was approximately 449,000 cycles for the WPI frame. The predicted number of cycles to failure for the heat-affected zone for the loading as defined by the test standard is 490,000 cycles. The data shows that the physical test and the predicted cycles to failure are similar (difference of 8.4%) which validates the accuracy of the FEA model. The second frame failed at roughly 300,000 equivalent cycles at the outside testing facility. The group observed that the second frame had a slightly different geometry when compared to the frame tested by the group. These differences included a difference in head tube length, and a difference in weld length between the top and down tube. Since the FEA was based on the frame tested at WPI, the cycles to failure prediction for the second frame was less accurate. However, there was still very good agreement between the FEA and physical frame testing for failure location and cycles to failure. This is especially true for the frame that the group tested.

4.2 Physical Frame Failure Analysis

In order to obtain an understanding of the fracture origin, propagation, and root cause, the group performed an extensive study on the crack. Crack propagation rates were measured for the entire crack length along with the location of the crack. It was also necessary to study both the fracture surface and the profile surrounding the fracture. This was accomplished by observing the crack on both a macroscopic and microscopic scale.

4.2.1 Observed Crack Propagation during Testing

Using simple observation during testing, the group saw the crack initiate on the bottom center of the top tube directly adjacent to the weld that joins the top tube and down tube together. This can be seen in Figure 46.

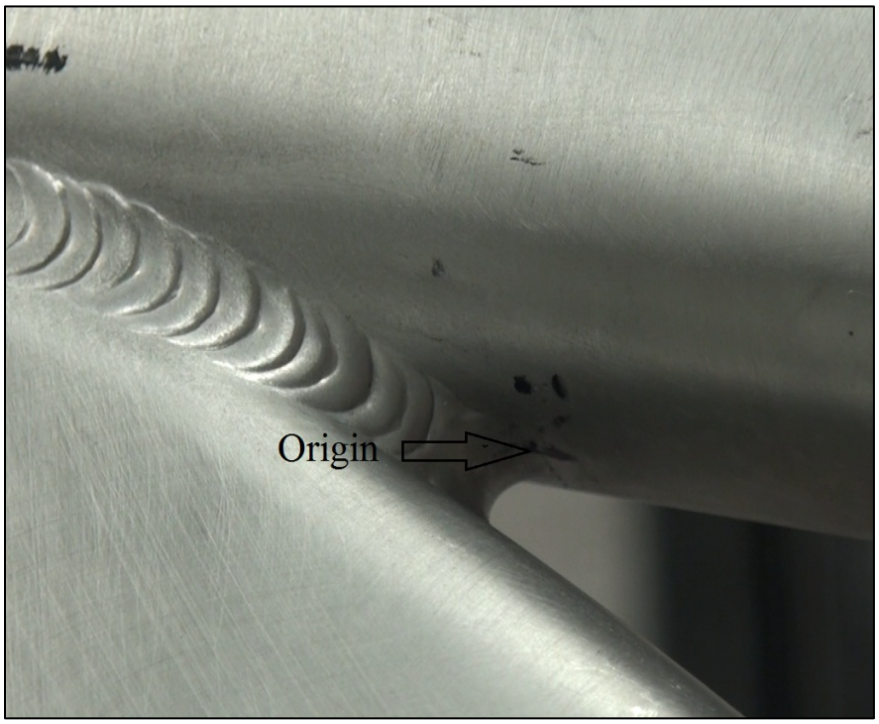

Figure 46: Fracture origin observed during testing.

This crack initiation point is in the weakest part of the HAZ. The crack then propagated straight up, on both sides of the top tube. It eventually stopped about two thirds of the way up on either side of the top tube. The extent that the crack propagated on one side of the top tube can be seen in Figure 47 with the head tube on the left side of the image.

Figure 47: Extent of crack propagation on front side.

4.2.2 Crack Growth Analysis

Length measurements of the crack were taken as it propagated through the frame. These measurements and the corresponding number of cycles are plotted in Figure 48. Each measurement point was defined by the group as a node, which allowed for correlation during fractographic analysis. The front side of the crack had 12 nodes, and the back side of the crack had 8 nodes.

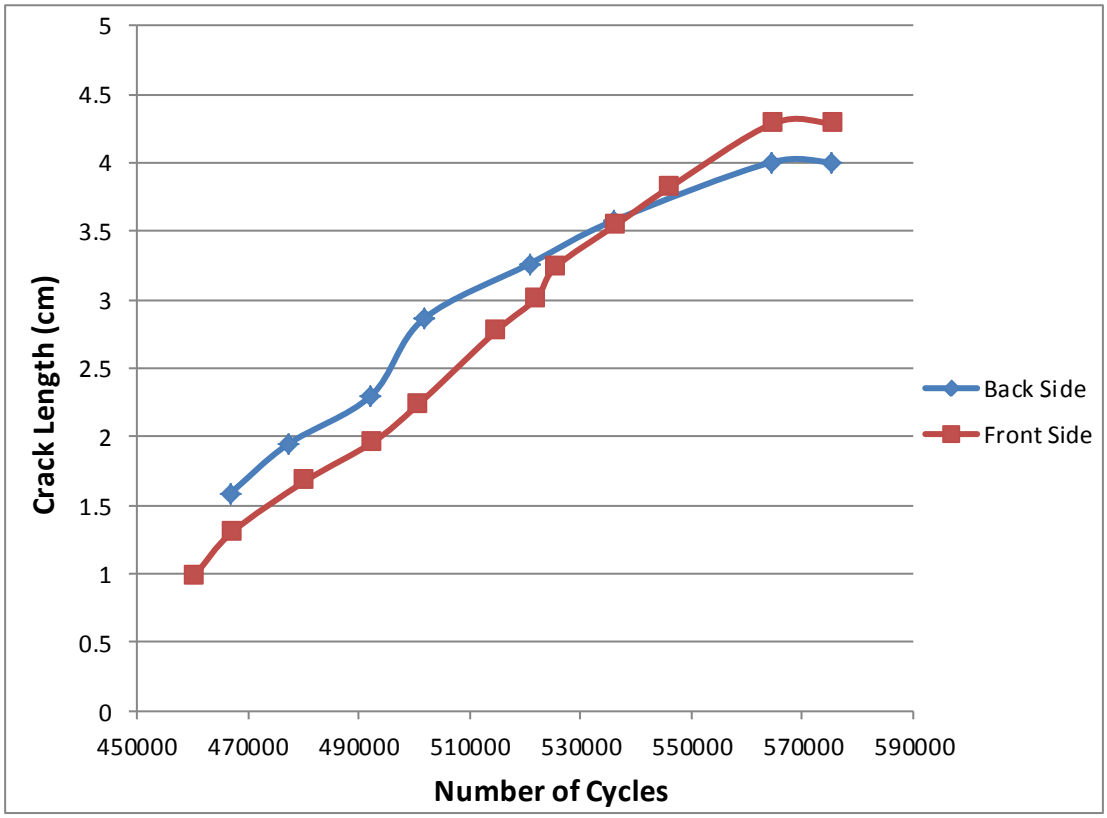

Figure 48: Crack lengths for front and back side at N cycles.

From Figure 48 it is clear that the crack growth rate is mostly linear on both the front and back side of the tube until approximately 570,000 cycles. The total crack length was then determined using the measurements on each side of the frame and can be seen in Figure 49.

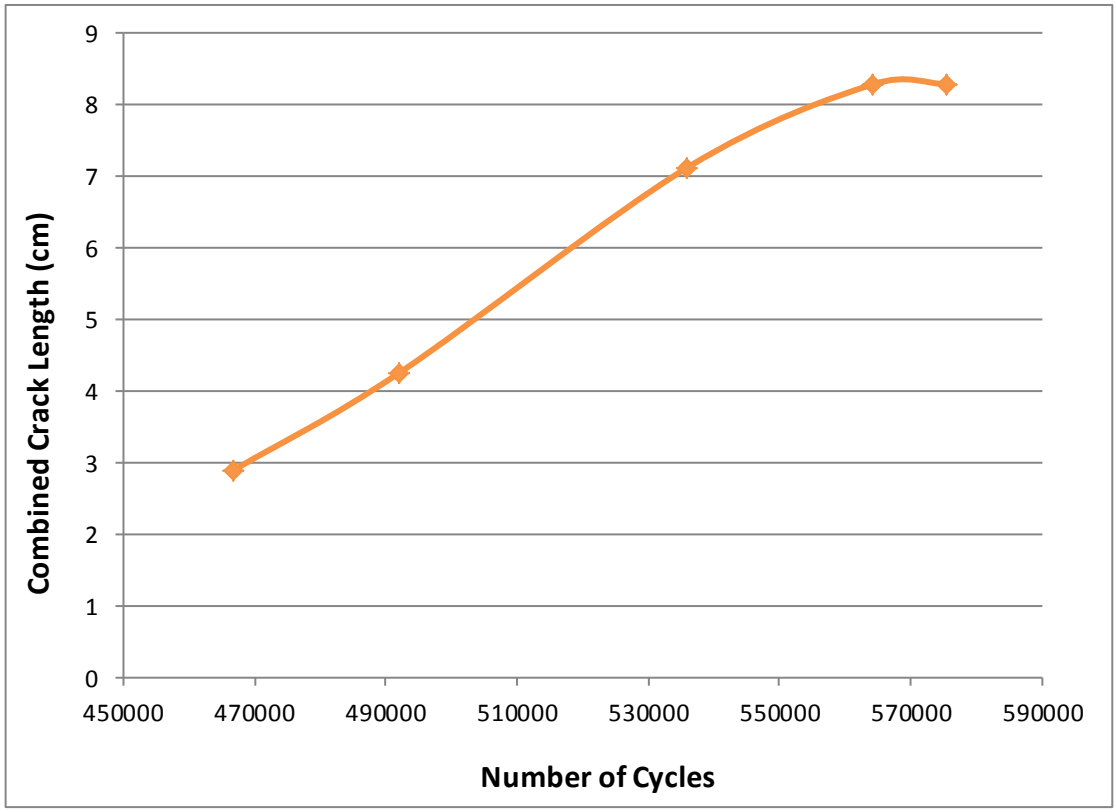

Figure 49: Combined crack length at N cycles.

As seen in Figure 49, the crack growth rate increased until approximately 540,000 cycles, and then slowed down until stopping at roughly 570,000 cycles. At this point the crack ceased to propagate with additional cycles. The growth rate for the entire length of the crack is seen in Figure 50.

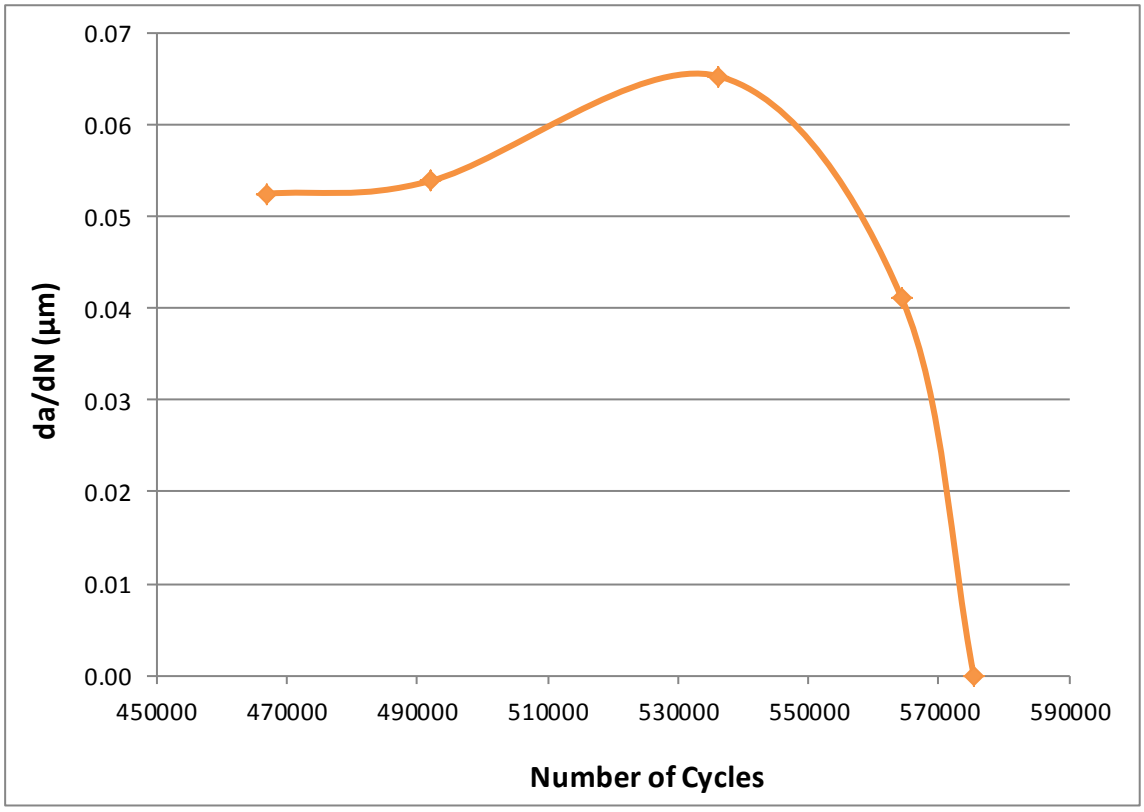

Figure 50: Combined crack growth rate at N cycles.

From Figure 50 it is clear that the crack growth rate increased until approximately 540,000 cycles. After this point, the crack growth rate rapidly decreased until the crack stopped propagating completely. This halt in propagation can be attributed to a lack of tensile stress in the upper portion of the top tube. When the frame was under maximum loading conditions, the lower portion of the top tube was in tension and the upper portion was in compression. When the crack moved into the portion of the frame in compression, it stopped propagating. Another contributing factor was the support provided by the down tube during tensile loading.

4.2.3 Fractographic Analysis

After failure, the crack surface was removed from the frame and analyzed on a microscopic scale. An optical microscope analysis was conducted, followed by a stereo microscope and SEM analysis. Images were taken during each of the analyses.

A natural light observation on the profile of the crack was used to identify how the crack interacted with the different phases in the material. Different phases within the material appeared as dark spots during the analysis, and interactions between the crack edge and these dark spots were observed.

The samples used for the profile investigation were then electrolytically etched and viewed under polarized light. The polarized light along with the electrolytic treatment exposed the grains of the metal so that the interaction between the grain boundaries and the crack edge could be observed.

Next, the face of the fracture surface was placed in the SEM with the primary goals of determining the actual initiation site as well as the striation distances at each of the nodes. A striation represents a microscopic gap caused by the physical advancement of the crack due to one loading cycle. A Jeol JSM 7000f SEM was used for the analysis. The fracture surface was viewed under a stereomicroscope as a preliminary to the SEM analysis. This allowed the group to readily identify areas of interest more easily than with the SEM. The fracture surface sample was cleaned ultrasonically with acetone prior to the SEM analysis.

In order to more completely understand how changes in striation distance affect crack growth rate; striation distances at each node had to be measured. At nodes 1 and 8 striations were not angled perpendicularly with the direction of crack propagation. At

these nodes, trigonometry was used to determine the equivalent perpendicular striation distance.

The resulting pictures from the fractographic analysis are summarized in Figure 51. As seen, the fracture analysis regions correspond to the nodes from the back side of the crack that were marked to evaluate crack growth as discussed in Section 4.2.2. The nodes analyzed were 1, 3, 5 and 8, and analyzing these nodes thoroughly characterizes the crack growth.

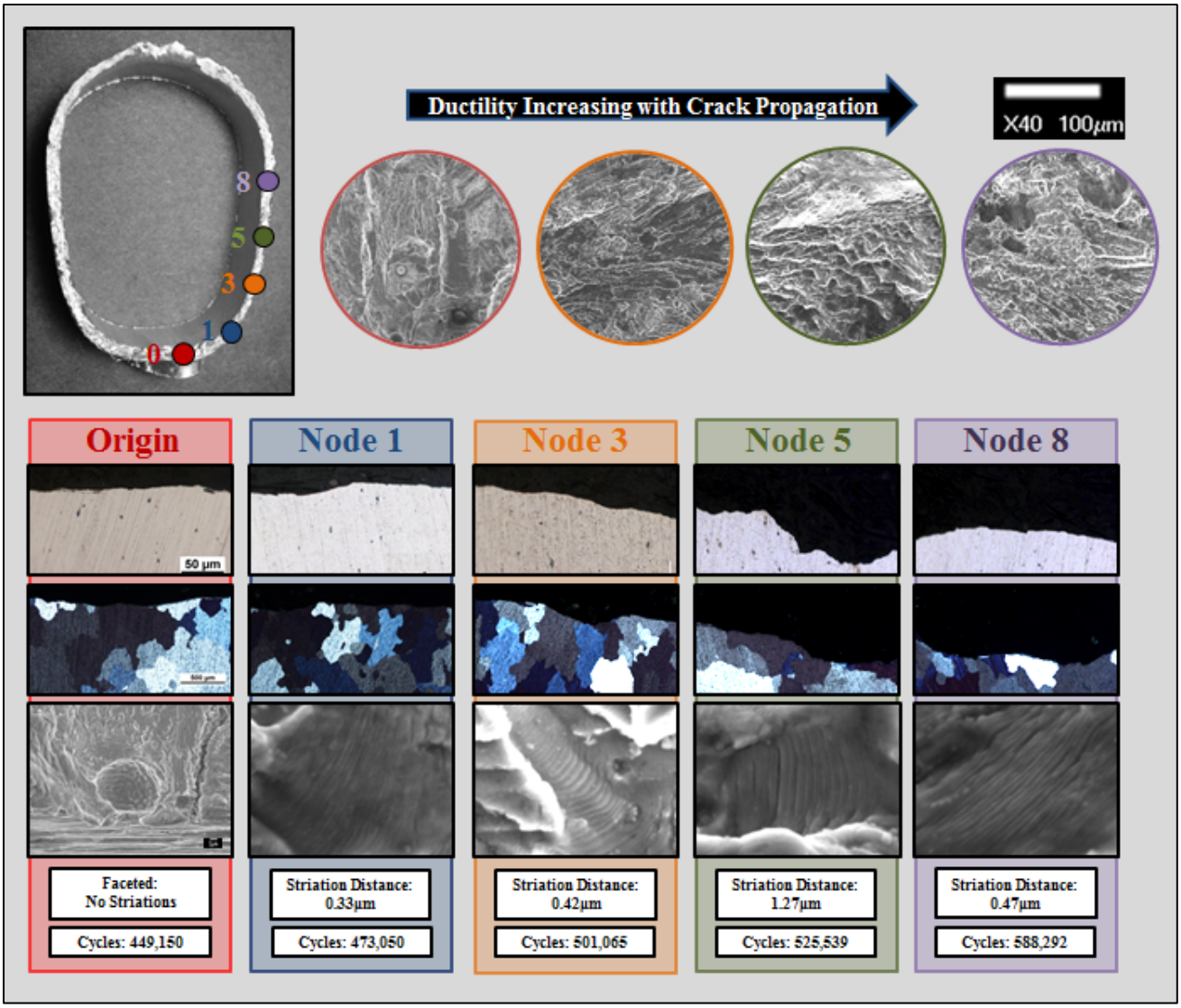

Figure 51: Results from optical microscope and SEM analysis.

The crack propagation observed by the group can be broken down into three sections. The beginning consisted of the origin and nodes 1 and 2, and featured a slow growth rate. The middle consisted of nodes 3-6, and featured faster crack propagation. Finally, the end of the crack growth consisted of nodes 7 and 8, and featured a growth rate similar to that of the beginning.

The propagation of the crack as viewed under the optical microscope can be seen directly below the node titles in Figure 51. The beginning of the crack growth featured propagation with little interaction with the different phases of the material. The next row of pictures shows that there was also limited interaction with the grain boundaries during this time of initial propagation. This corresponds to a transgranular mode of crack growth. The final row of pictures shows the fracture surface as viewed under the SEM. Small distances between the striations can be seen in the beginning phase which corresponds to the slow crack growth that was observed. The middle section features more substantial interaction with the phases and grain boundaries of the material. This intergranular mode of propagation along with the large striation distances seen at these nodes alludes to the fast growth rate that was observed. In the end, as the propagation began to slow down, the crack transitioned back to having limited interaction with the phases and grain boundaries. This shift to transgranular propagation along with the small striation distances coincide with slower crack growth rates.

By tracing the striations, and observing defects in the material using the SEM, the group was able to identify a crack origin point on the fracture surface. The origin point was a feature that appeared to be a porosity near the outer edge of the tube where the

team first observed the crack. This porosity was in the HAZ, and had high levels of tensile stress shown in the FEA which make it the likely origin.

Fracture Data

The predicted striation distances for the crack and the stress intensity factors were calculated to aid in the analysis of the crack. In order to predict striation distance, da/dN, changes in crack length were divided by changes in the number of cycles at their respective nodes. In areas of more rapid crack growth, striation distances were predicted to be larger. These values, along with the observed striation distance, can be seen in Table 11.

The applied stress, σ, taken directly from the FEA, along with the crack length, a, was used to calculate the stress intensity factor, K_C, using the equation below. The stress intensity factor characterizes the stress at the tip of the crack. These values can be seen in the right column, along with the change in stress intensity factor in Table 11.

$$K_c \approx \sigma\sqrt{\pi * a}$$

Table 11: Fracture data and calculations

Node (Back Side)	Cycles (N)	dN	Crack Length (cm)	Change in Crack Length (cm)	da/dN	Observed Distances Between Striations (μm)	Applied Stress (Mpa)	K_c (MPa*m^.5)	ΔK_c (MPa*m^.5)
1	574,084		1.32			0.329	89.8	18.29	
2	591,806	17,722	1.59	0.27	0.15	0.424	81.7	18.23	-0.06
3	602,099	10,293	1.94	0.36	0.345	0.424	57.2	14.12	-4.11
4	617,144	15,045	2.30	0.36	0.236	0.939	40.8	10.97	-3.15
5	626,573	9,429	2.86	0.56	0.593	1.27	24.5	7.34	-3.63
6	645,710	19,137	3.26	0.40	0.211	1.17	8.17	2.62	-4.73
7	661,006	15,296	3.58	0.32	0.208	0.75	6.17	2.07	-0.55
8	689,326	28,320	4.00	0.42	0.15	0.469	1.63	5.79	3.73

As seen in Table 11, the applied stress acquired from the FEA drops greatly as the crack progresses. This is due to the complex geometry of the tube and compressive loading seen in the FEA output on the top of the top tube. Due to this drop in applied stress during crack progression, the derived stress intensity factors are abnormal in comparison to data resulting from a crack formed during a standard fatigue test on a uniform bar. Typically in these experiments the change in stress intensity factor and da/dN increases with crack propagation, unlike what was seen on the bike frame.

Striation Distance Comparison (Predicted vs. Measured)

Charts showing the comparison between the calculated "predicted" striation distances and the measured striation distances can be seen in Figure 52. The two charts use the data from Table 11 and a trend line to allow visualization of the change in striation distance.

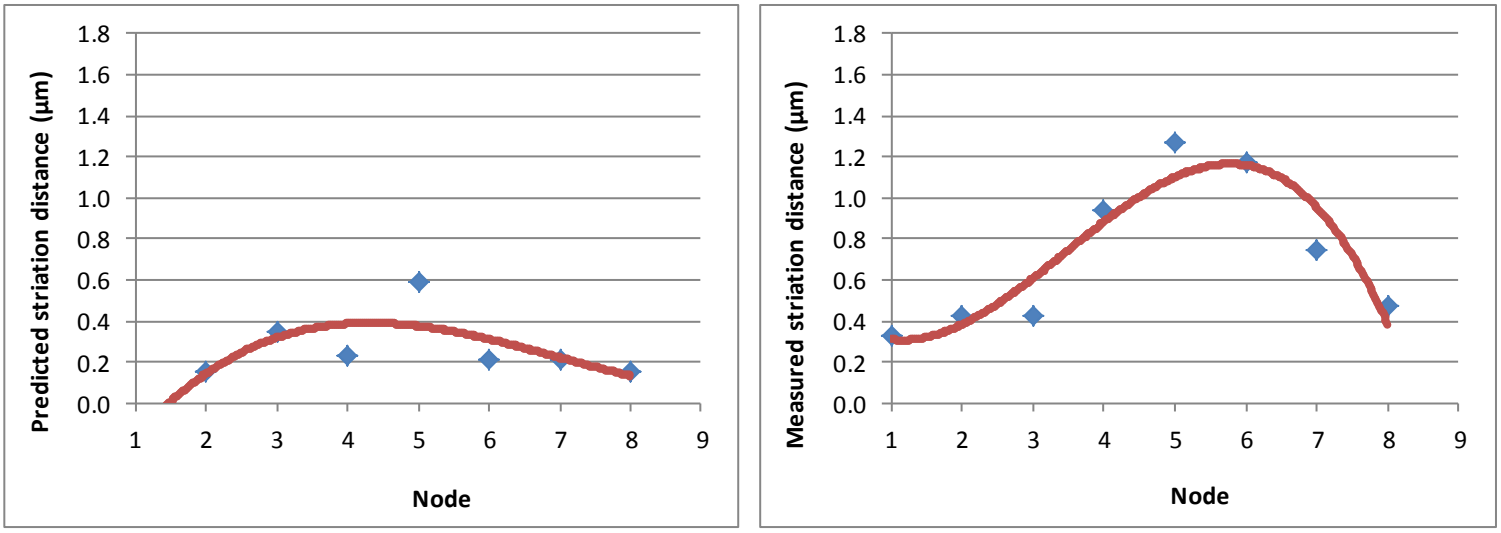

Figure 52: Predicted (left) and measured (right) striation distance.

The similar trends between graphs indicate a clear correlation between change in crack length per change in cycle and the striation distances at certain nodes along the crack. Points along the fracture that have large distances between striations have a large change in crack length per cycle and points that have small distances between striations have small changes in crack length per cycle, as would be expected. As seen, the magnitude of striation distance is different between the predicted and measured. This may be attributed to a slight error in measuring striation distance, or in the accuracy of the crack length measurements.

5.0 Frame Optimization and Recommendations

After creating the FEA model, validating it with physical testing, and conducting a fractographic analysis of the crack, modifications were made to attempt to improve fatigue life and optimize the frame. Even though the frames lasted almost eight times the ASTM test standard requirement, the group worked to provide recommendations to the bike manufacturer to aid them with their goal of producing bikes that can withstand abusive riding conditions without failure. The group explored optimizations targeted at material, heat treatment, and geometry modifications.

5.1 Material Modifications

The group explored two different aluminum alloys with the same frame design to improve fatigue life. The group investigated 7005 aluminum, a common bicycle frame material, and 6013 aluminum, a relatively new aerospace alloy.

5.1.1 7005-T6 Aluminum

The 7005-T6 aluminum alloy is commonly used for mountain bike frames. Based on the data from Table 2, the ultimate tensile strength of 7005-T6 is roughly 10%more than 6061-T6. Since 7005 is not common outside of the bicycle industry, an S-N chart for the material could not be found. Therefore, the group made the assumption that the fatigue life for 7005-T6 is 10% longer than that of 6061-T6.

5.1.2 6013-T6 Aluminum

The 6013-T6 aluminum alloy was another material that the group investigated for the bicycle frame. This alloy is a relatively new alloy that provides favorable tensile strength and fatigue failure resistance compared to 6061-T6. The alloy composition for 6013 can be seen below in Table 12. As seen in the table, 6013 has much lower iron content than 6061, and much higher copper content. The low iron content would likely increase fatigue life, as stress concentrations caused by the iron phases would decrease.

The high copper content in 6013-T6 indicates high fatigue life and strength. Since there is higher copper content compared to 6061, more copper-aluminum precipitates ($CuAl_2$) form to complement the magnesium-silicon precipitates formed during artificial aging. There are similar magnesium and silicon levels in 6061 and 6013, which likely indicates the same amounts of magnesium-silicon precipitates. Both of these precipitates aid in strengthening the material and improving fatigue life because the precipitates restrict dislocation movement in the metal [17].

Table 12: Approximate chemical composition of 6013 by wt% [16]

Al	Mg	Cu	Si	Mn	Fe	Zn	Cr	Ti	Others
~96.1	0.95	.9	.75	0.35	0.30	0.25	0.1	0.1	.25

The mechanical properties of 6061-T6 and 6013-T6 are shown in Table 13. As seen in the table, 6013-T6 has a relatively similar modulus of elasticity and density to 6061-T6. Since the modulus of elasticity and density is roughly the same, the frame would likely have the same “feel” to a rider, which for many riders is highly important. The 6013-T6 alloy has a yield strength and ultimate tensile strength that are 32% higher

than 6061-T6, and a fatigue strength that is nearly 50% higher than 6061-T6. This increase in strength would ensure the frame would fail under higher loading, and would require more cycles to fail.

Table 13: Comparison of mechanical properties between 6061-T6 and 6013-T6 [16]

Material	Modulus of Elasticity (GPa)	Yield Strength (MPa)	Ultimate Tensile Strength (MPa)	Fatigue Strength at 50,000 Cycles (MPa)	Density (kg/m^3)	Cost (USD per kg)
6061-T6	72	250	280	95	2700	$2.42
6013-T6	70	330	370	140	2710	$2.42

An FEA was conducted using the material properties of 6013-T6 in place of 6061-T6. The stress output on 6013-T6's S-N curve can be seen in Figure 54.

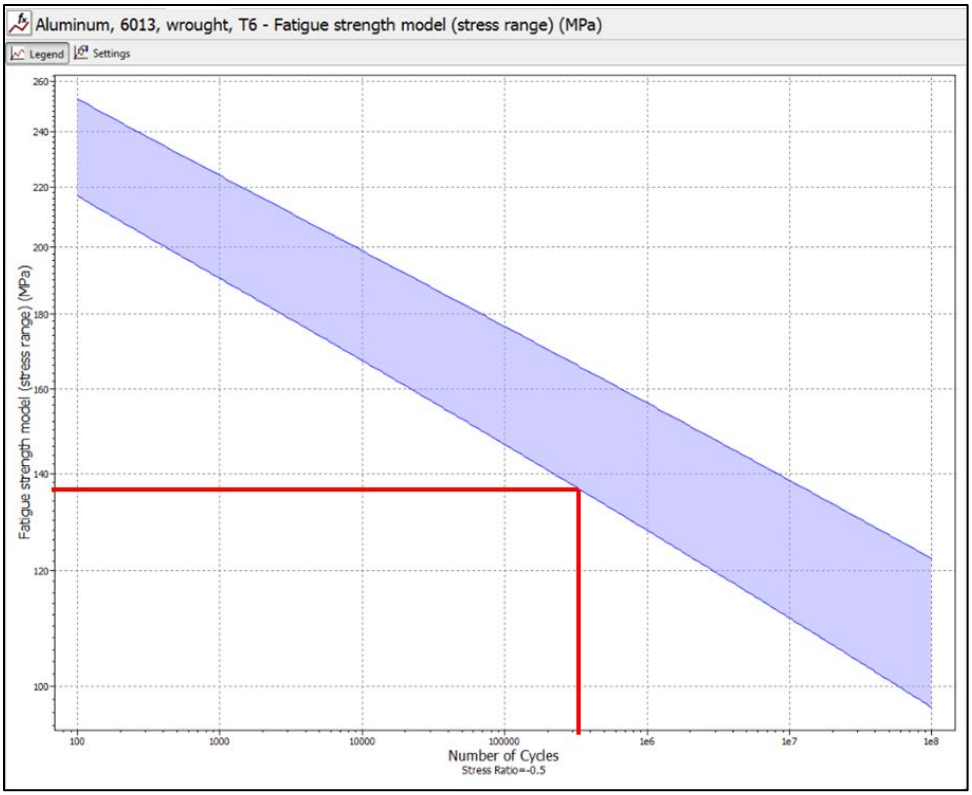

Figure 53: Aluminum 6013-T6 S-N curve showing extended fatigue life.

It can be seen that the fatigue life of 6013-T6 is extremely high. With a fatigue life of ~2,000,000 cycles, fatigue failure is not an issue that is likely to occur during a bicycle frame's lifetime. However, the main drawback to 6013-T6 is that it is not as readily available as 6061. As of 2012, tubing could only be purchased in large quantities for this alloy, making 6013-T6 a viable option for fatigue life improvement, as long as high quantities of the alloy are purchased.

5.1.3 Heat Treat Modifications

The group investigated alternative heat treatments for the 6061 bicycle frame. The T4 and T7 temper heat treatments were chosen to be investigated, as they are common heat treatments for 6061.

- **T4 Heat Treatment**: The T4 heat treatment utilizes a solution heat treatment with natural aging to bring the alloy to a stable condition. This differs from T6 heat treatment as the T4 heat treatment does not include an artificial aging. The S-N curves for a T4 heat treatment show that the process yields far lower fatigue strength for a given stress compared to the T6 heat treatment. Since the T4 heat treatment is not a precipitation hardening heat treatment, the precipitates that strengthen the material during the artificial aging with a T6 and T7 heat treatment do not form. These precipitates generally strengthen the material, reducing dislocations which cause failure [18].
- **T7 Heat Treatment**: The T7 heat treatment is a solution heat treatment followed by overaging. This overaging process involves high artificial aging temperatures after the material is quenched. The T7 heat treatment, like the T6 heat treatment,

is a precipitation hardened heat treatment. Investigation into the use of T7 heat treatment using the ASM Handbooks allowed for the conclusion that this overaging process generally sacrifices strength for dimensional stability and corrosion resistance. Since dimensional stability and corrosion resistance are not prominent issues, this heat treatment was not found to be beneficial for fatigue life [18].

The material and heat treatment optimization investigation results can be seen below in Table 14. As shown, both heat treatment adjustments had a negative effect on fatigue life, as discussed above, and the material changes had a positive effect. The 6013-T6 material had a significantly higher fatigue life and is thus the optimal modification.

Table 14: Material and heat treatment optimization results

Modification	Cycles to Failure	Predicted Failure Location	Cost
6061-T6 (current)	~490,000	Top tube near head tube or down tube near bottom bracket	No change
6013-T6	**~2,000,000**	**Down tube near bottom bracket**	**No change** *(bulk purchase required)*
7005-T6	~495,000	Top tube near head tube	~10% more than 6061
T4 heat treatment	~5,500	Top tube near head tube	No change
T7 heat treatment	~300,000	Top tube near head tube	No change

5.2 Geometry Modifications

5.2.1 Extend Length of Weld Between Top and Down Tube

The radius of curvature of the upper section of the down tube and the length of the weld were modified to improve the fatigue life of the frame. The modifications to the frame can be seen in Figure 55. The radius of curvature of the down tube was increased, and the length of the weld was increased by 50%. The group hypothesized that by increasing the radius of curvature of the down tube, the stress levels will decrease. This hypothesis was validated using an FEA model of the modified frame. The extended weld allows for the load transmission to dissipate over a larger area on the top tube, also reducing stress levels.

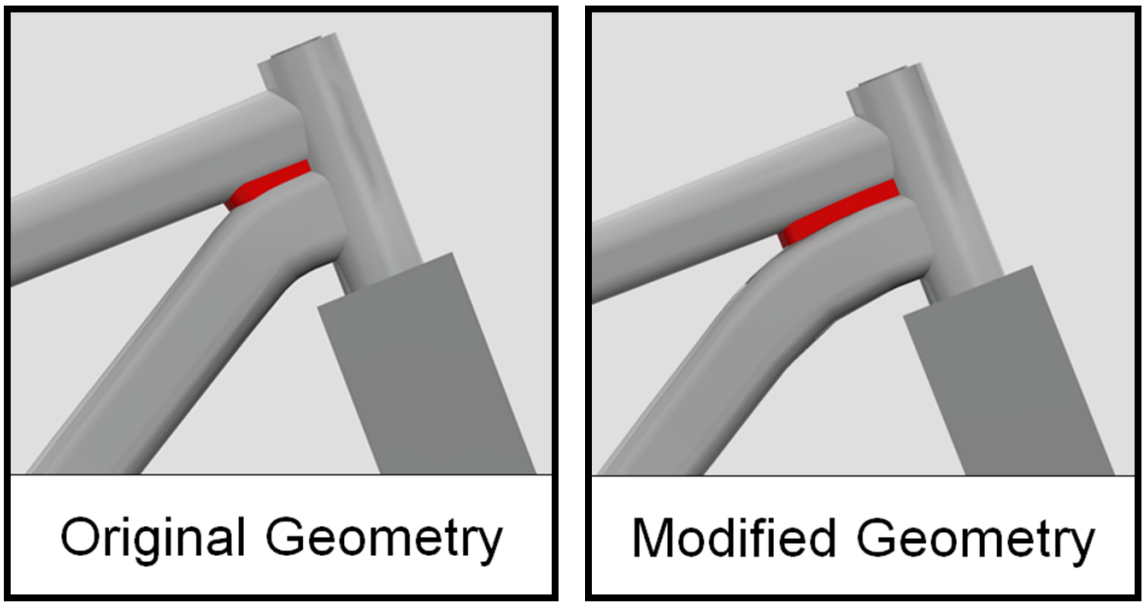

Figure 54: Frame geometry modification showing extended weld.

5.2.2 Adjust Thickness of Down Tube

The thickness of the down tube near the bottom bracket was increased by 50%. Since the failure on the frame sent out for third party testing happened in this location, and the FEA showed high tensile stress in this area, the group determined adjusting this area would be effective. The thickness was adjusted from 1.01 mm near the bottom bracket to 1.52 mm. The results for the optimization investigation can be seen in Table 15.

Table 15: Geometry optimization results

Modification	Cycles to Failure	Predicted Failure Location
Current geometry	~490,000	Top tube near head tube or down tube near bottom bracket
Extend weld length between top and down tubes	~300,000	Down tube near head tube
Adjust thickness of down tube near BB	~400,000	Top tube near head tube
Combined weld extension and adjusted thickness	**~600,000**	**Down tube near bottom bracket**

5.2.3 Recommendation Summary

An investigation was conducted with the optimal material / heat treatment, and geometry design. The optimal 6013-T6 alloy was set for the frame material. The geometry was optimized with the extended weld between the top and down tube, increased radius of curvature for the down tube, and increased down tube thickness near the bottom bracket. The results from the investigation are seen in Table 16.

Table 16: Modification summary for optimal fatigue behavior

Modification	Cycles to Failure	Predicted Failure Location
6061-T6 and current geometry	~490,000	Top tube near head tube or down tube near bottom bracket
6013-T6 and current geometry	~2,000,000	Down tube near bottom bracket
6061-T6 and modified geometry	~600,000	Down tube near bottom bracket
6013-T6 and modified geometry	**~3,500,000**	**Down tube near bottom bracket**

As seen in Table 16 the fatigue life with the optimal model was predicted to be approximately 3,500,000 cycles by the FEA. The failure location was predicted to be on the down tube near the bottom bracket. This location is significantly safer than the head tube region, as a failure would not cause the ride to fall going over the front handlebars.

6.0 Conclusions and Future Work

In conclusion, the group successfully characterized the fatigue behavior of the donated bicycle frames, and optimized the frame material, heat treatment, and geometry to improve fatigue life. The finite element methodology proved to be an accurate way of predicting fatigue failure locations and cycles to failure. This was validated based on the methodology agreeing with the physical testing results. The fatigue failure locations were almost exactly the same between the FEA and physical testing, and the cycle count was within a 10% difference. The fractographic analysis allowed for an accurate characterization of the fracture and origination point, and a thorough understanding of the crack growth.

The group was able to optimize the bike frame which resulted in a predicted fatigue life that is approximately 3,500,000 cycles compared to 490,000 for the original frame The group recommends that future work be done to investigate 6013-T6 aluminum. The group also recommends extending the weld between the top and down tubes and increasing the thickness of the down tube. The FEA methodology and physical frame testing rig described in this report could be used to investigate these modifications to determine their effectiveness in a future project.

7.0 Acknowledgements

The group would like to extend a special thank you to the following people who helped the group successfully complete the project:

Professor Diana A. Lados

Sinister Bikes

Torbjorn Bergstrom

Xiang Chen

Stephen Cialdea

Michael Fagan

Anastasios Gavras

Dr. Adriana Hera

Nate Jannetti

Jonathan Leith

James Loiselle

Bradford Lynch

Professor Robert L. Norton

Randy Robinson

Adam Sears

Professor John M. Sullivan

Mike Zancanato

Appendix A – T6 Heat Treatment Parameters

Below are the parameters for a T6 heat treat for 6061 aluminum.

Thickness, mm (in.)	Soak time in minutes				Maximum Quench Delay in Seconds
	Air Furnace		Salt Bath		
	Min	Max	Min	Max	
≤0.41 (0.016)	20	25	10	15	5
0.51 (0.020)	20	30	10	20	7
0.64 (0.025)	25	35	15	25	7
0.81 (0.032)	25	35	15	25	7
1.02 (0.040)	30	40	20	30	10
1.27 (0.050)	30	40	20	30	10
1.35 (0.053)	30	40	20	30	10
1.80 (0.071)	35	45	25	35	10
2.03 (0.080)	35	45	25	35	10
2.29 (0.090)	35	45	25	35	10
2.54 (0.100)	40	55	30	45	15
3.18 (0.125)	40	55	30	45	15
4.06 (0.160)	50	60	35	45	15
4.57 (0.180)	50	60	35	45	15
6.35 (0.250)	55	65	35	45	15
>6.35 (0.250)-12.7 (0.500)	65	75	45	55	15
For each additional 12.7 (1/2) or fraction	30	30	20	20	15
Rivets (all)	60	…	30	…	5

Appendix B – Solenoid Controller LabVIEW VI

Below is the VI block diagram in National Instruments LabVIEW used to control the solenoid valves.

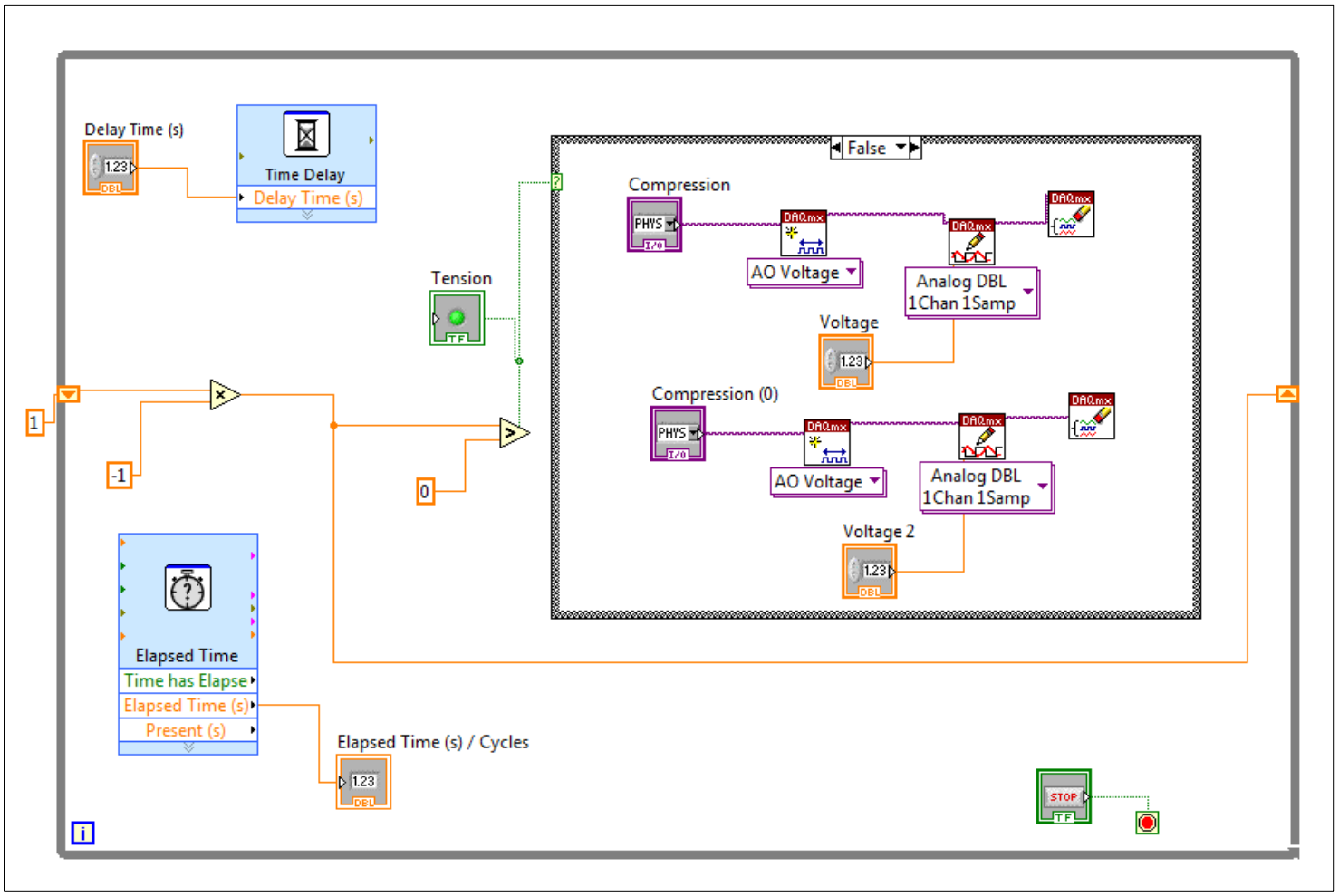

Appendix C – Strain Measurement LabVIEW VI

Below is the VI block diagram in National Instruments LabVIEW used to measure the strain on the bicycle frame during testing.

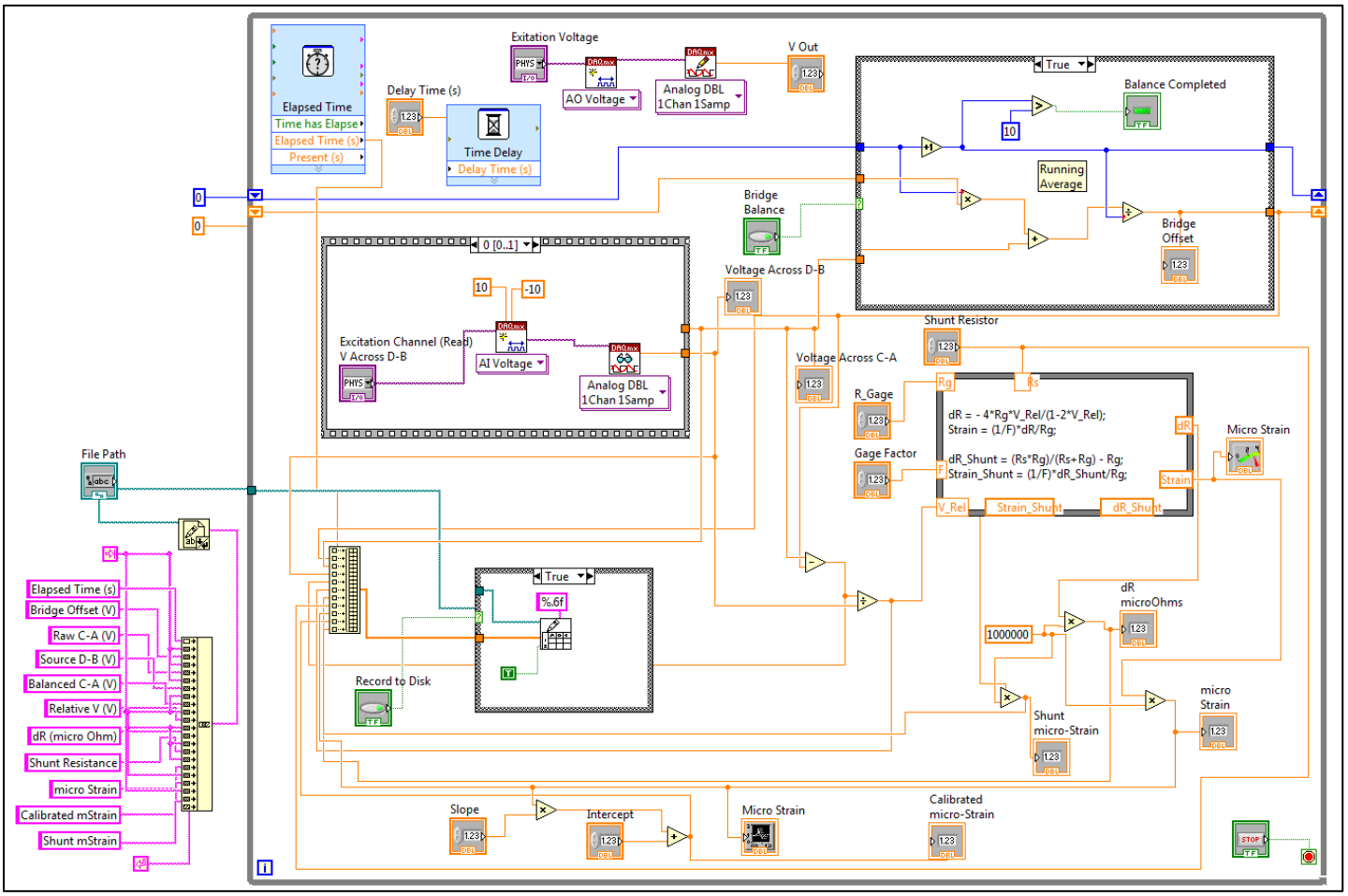

Appendix D – Air Cylinder Force Output Graphs

Below are the graphs used to determine the air pressures for the air cylinder.

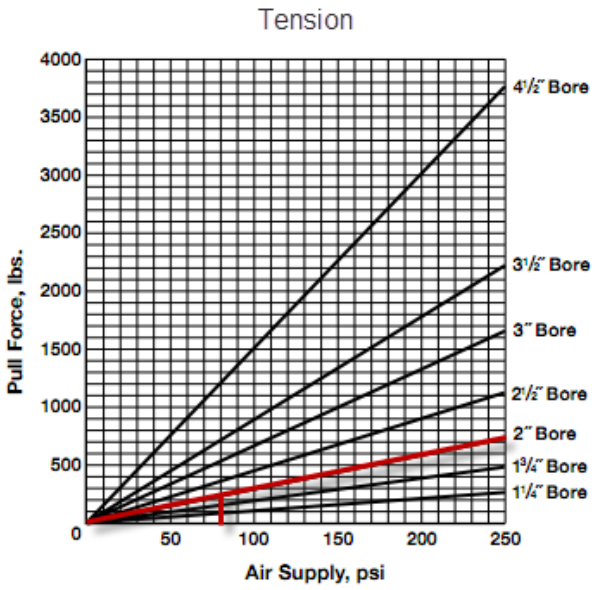

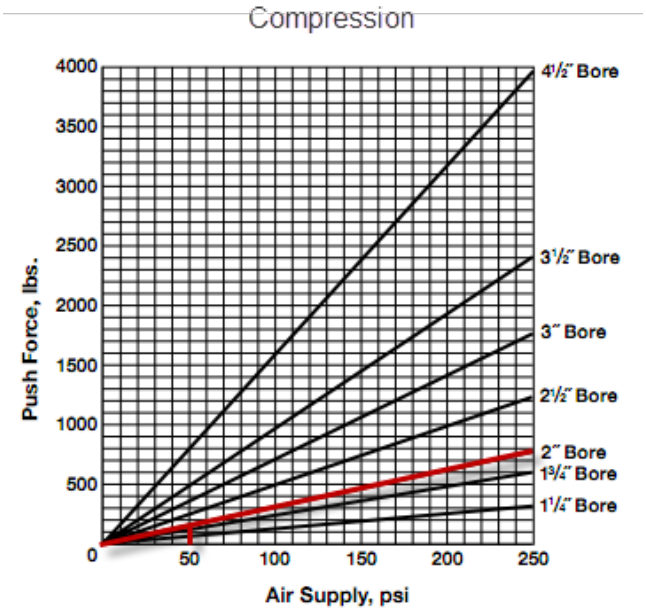

Appendix E – ASM Material Hardness Reference

Below is a graph from the ASM Handbook which the group used as a reference for the Rockwell hardness tests.

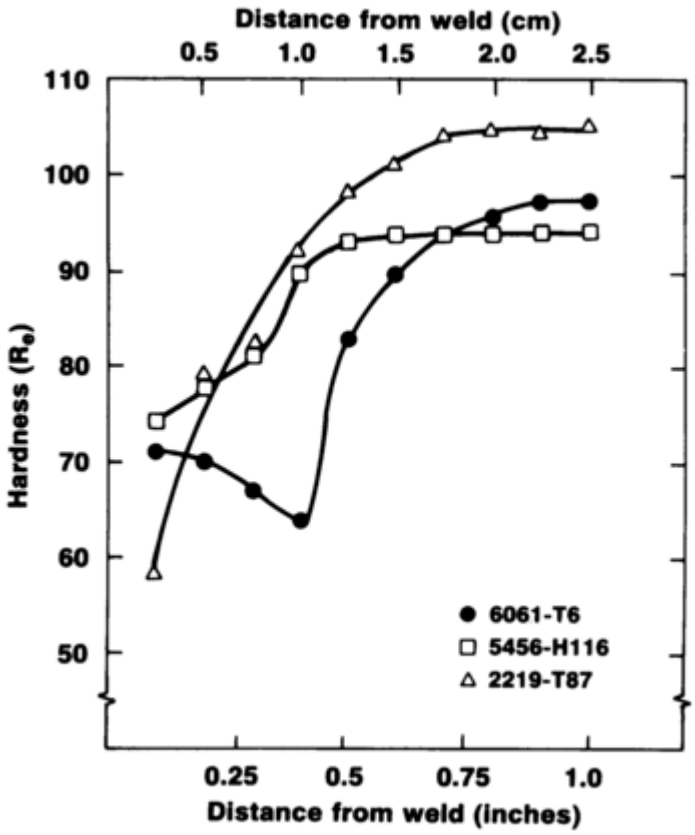

References

1) "80/20 Inc. - The Industrial Erector Set." 80/20 Inc. - The Industrial Erector Set. Web. Accessed 12 Oct. 2011. <http://www.8020.net/T-Slot-2.asp>.

2) Alcoa. "Understanding Extruded Aluminum Alloys." Alcoa.com. Dec. 2002. Web. Accessed 14 Oct. 2011. <http://www.alcoa.com/adip/catalog/pdf/Extruded_Alloy_6061.pdf>.

3) "Aluminum Tube-how it attains its shape". Aluminum Global Suppliers. Accessed 15 Dec. 2011 <http://www.aluminiumglobalsuppliers.com/manufacturing/aluminium-tubes.shtml>.

4) ASTM Standard F2043-09, "Standard Classification for Bicycle Usage," ASTM International, West Conshohocken, PA, www.astm.org.

5) ASTM Standard F2614-09, "Standard Specification for Condition 3 Bicycle Frames," ASTM International, West Conshohocken, PA, www.astm.org.

6) ASTM Standard F2711-08, "Standard Test Methods for Bicycle Frames," ASTM International, West Conshohocken, PA, www.astm.org.

7) ASTM Standard F2802-09, "Standard Specification for Condition 1 Bicycle Frames," ASTM International, West Conshohocken, PA, www.astm.org.

8) ASTM Standard F2843-10a, "Standard Specification for Condition 0 Bicycle Frames," ASTM International, West Conshohocken, PA, www.astm.org.

9) ASTM Standard F2868-10, "Standard Specification for Condition 2 Bicycle Frames," ASTM International, West Conshohocken, PA, www.astm.org.

10) Brown, Sheldon. "Frame Materials for the Touring Cyclist." Sheldon Brown-Bicycle Technical Information. Sheldon Brown, Aug. 2010. Web. Accessed 06 Sept. 2011. <http://www.sheldonbrown.com/frame-materials.html>.

11) Brown, Sheldon. "Glossary: Diamond Frame". Accessed 04 Oct. 2011.

12) "CPSC And Cannondale Announce A Bicycle Frame Safety Inspection Program." U.S. Consumer Product Safety Commission. CPSC, 25 01 1995. Web. Accessed 18 Sept. 2011 <http://www.cpsc.gov/cpscpub/prerel/prhtml95/95069.html>.

13) "CPSC, Recreational Equipment Inc. Announce Recall of Children's Bicycles." U.S. Consumer Product Safety Commission. December 2005 Web. Accessed 18 Sept. 2011 <http://www.cpsc.gov/cpscpub/prerel/prhtml06/06520.html>.

14) Failure Analysis and Prevention, ASM Metals Handbook, Vol 11, 1983, p 378.

15) "Friction Stir Welding Applications." TWI. Web. Accessed 22 Sept. 2011. <http://www.twi.co.uk/content/fswapp.html>.

16) GRANTA. 2011. CES EduPack. Granta.

17) Heat Treating of Aluminum Alloys, Heat Treating, Vol 4, ASM Handbook, ASM International, 1991.

18) Heat Treating of Aluminum Alloys, Properties and Selection: Nonferrous Alloys and Special Purpose Materials, Vol 2, ASM Handbook, ASM International, 1991.

19) http://spaceflight.esa.int/impress/text/education/Images/MechanicalProperties/Image046.png. Accessed 10 Oct. 2011.

20) http://svana.org/photos/singlespeed_mtb/websize/new_steel_mtb_frame.jpg. Accessed 10 Oct. 2011.

21) http://www.burls.co.uk/images/ti/largeMTB.jpg. Accessed 10 Oct. 2011.

22) http://www.kirkframeworks.com/images/JK_cross/JKC_miter/DSC_1415.jpg. Accessed 10 Oct. 2011.

23) Kalpakjian, Serope erope, and Steven teven R. chmid. Manufacturing Processes For Engineering Materials. 5th. Prentice Hall, 2008. Print.

24) Kuhn, Howard, and Dana Medlin. Mechanical Testing and Evaluation. Materials Park, OH: ASM International, 2000. Print.

25) Lang, L. H. "Hydroforming Highlights: Sheet Hydroforming and Tube Hydroforming." Journal of Materials Processing Technology 151.1-3 (2004): 165-77. Print.

26) "Material Property Data." MatWeb. Web. Accessed 14 Oct 2011. <http://www.matweb.com/>.

27) Metallography: An Introduction, Metallography and Microstructures, Vol 9, ASM Handbook, ASM International, 2004, p 3-20

28) "Metals – Aluminum." Bikepro. Web. Accessed 15 Sept. 2011. <http://www.bikepro.com/products/metals/alum.html>.

29) "Microstructure Classification of Friction Stir Welds." TWI. Web. Accessed 22 Sept. 2011 <http://www.twi.co.uk/content/fswqual.html>.

30) Nelson, Ron. "Bike Frame Races Carbon Consumer Goods Forward." Reinforced Plastics. 47.7 (2003): 36-40. Web. Accessed 6 Sep. 2011.

31) "Niner Bikes Recalls Bicycle Frame Due to Crash Hazard." U.S. Consumer Product Safety Commission. May 2010 Web. Accessed 18 Sept. 2011 <http://www.cpsc.gov/cpscpub/prerel/prhtml10/10231.html>.

32) "Norco Recalls Bicycle Frames Due to Crash Hazard." U.S. Consumer Product Safety Commission. May 2009 Web. Accessed 18 Sept. 2011 <http://www.cpsc.gov/cpscpub/prerel/prhtml09/09223.html>.

33) "Parts of a Bicycle." The Bike Tube. Web. Accessed 18 Sept. 2011. <http://thebiketube.com/bike/frame>.

34) "Rockwell Hardness Testing" Materials Evaluating and Engineering, Inc. Web. Accessed 15 Nov. 2011 <http://mee-inc.com/rockhar.html>.

35) Santacruzbicycles.com. Accessed 14 Oct. 2011.

36) "Seattle Bike Supply is Voluntarily Recalling all 2008 Redline D640 Bicycles." Redline Bicycles. December 2010 Web. Accessed 18 Sept. 2011 <http://www.redlinebicycles.com/news/885-recall-notice-2008-d640>.

37) Sinisterbikes.com. Accessed 14 Oct. 2011.

38) "TIG Welding Aluminum bike Frame." Welding Tips and Tricks. Web. 20 Sept. 2011. <http://www.weldingtipsandtricks.com/tig-welding-aluminum-bike-frame.html>.

39) Trekbikes.com. Accessed 14 Oct. 2011.

40) "Understanding Bike Frame Materials." Brightspoke. Web. 06 Sept. 2011. <http://www.brightspoke.com/c/understanding/bike-frame-materials.html>.

41) Welding, Brazing and Soldering, ASM Metals Handbook, Vol 6, 1983, p 182

42) "What is Friction Stir Welding." ESAB Welding and Cutting. ESAB, n.d. Web. Accessed 22 Sept. 2011. <http://esabna.com/us/en/education/knowledge/qa/What-is-friction-stir-welding-of-aluminum.cfm>.

43) www.supplierlist.com/photo_images/25947/Carbon_fiber_bicycle_frame_manufaturer_monocoque_.jpg. Accessed 10 Oct. 2011.